Cell Reports

Article

Endosomal Dysfunction Induced by Directly Overactivating Rab5 Recapitulates Prodromal and Neurodegenerative Features of Alzheimer's Disease

Graphical Abstract

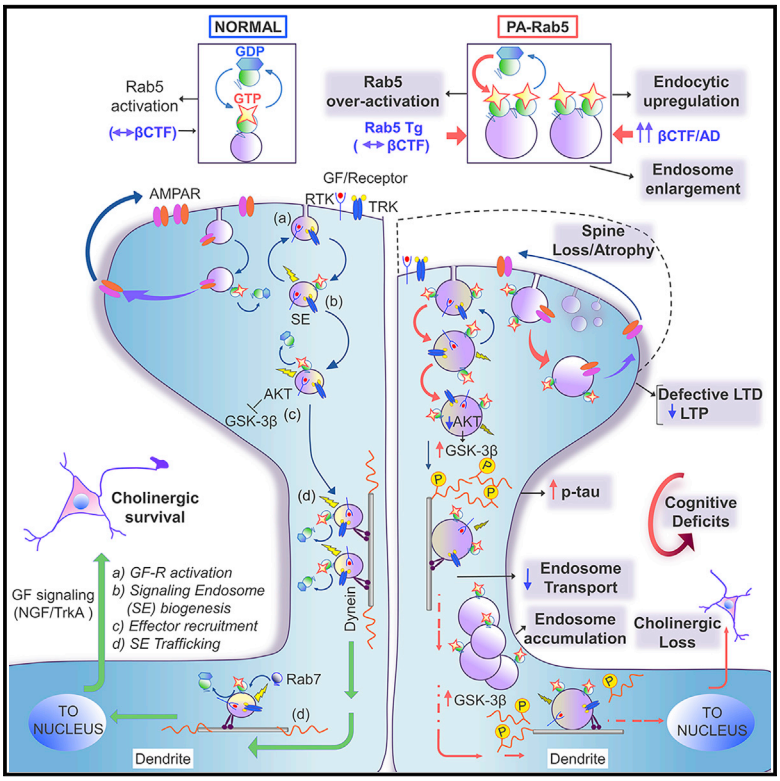

Highlights

- Pathological Rab5 activation in PA-Rab5 mice mimics AD-like endosomal dysfunction
- PA-Rab5 mice have synaptic function/structure deficits and GSK-3β-mediated tauopathy
- Rab5 overactivation *in vivo* underlies cholinergic degeneration and memory deficits
- Endosomal dysfunction alone induces prodromal and degenerative AD-related changes

Authors

Anna Pensalfini, Seonil Kim, Shivakumar Subbanna, ..., John F. Smiley, Balapal S. Basavarajappa, Ralph A. Nixon

Correspondence

ralph.nixon@nki.rfmh.org

In Brief

Pensalfini et al. generate mice reproducing neuron-specific pathological Rab5 activation (PA-Rab5) and elevated Rab5 expression as seen in AD, but independently of elevating APP-βCTF, its established trigger in AD. Rab5-mediated endosomal dysfunction drives a diverse prodromal/neurodegenerative cascade, independently of β-amyloid, suggesting that Rab5 may be a potential therapeutic target.

Pensalfini et al., 2020, Cell Reports *33*, 108420
November 24, 2020
https://doi.org/10.1016/j.celrep.2020.108420

CellPress

Cell Reports

CellPress
OPEN ACCESS

Article

Endosomal Dysfunction Induced by Directly Overactivating Rab5 Recapitulates Prodromal and Neurodegenerative Features of Alzheimer's Disease

Anna Pensalfini,[1,2] Seonil Kim,[3,10] Shivakumar Subbanna,[4] Cynthia Bleiwas,[5] Chris N. Goulbourne,[1] Philip H. Stavrides,[1] Ying Jiang,[1,2] Ju-Hyun Lee,[1,2] Sandipkumar Darji,[1] Monika Pawlik,[1] Chunfeng Huo,[1] James Peddy,[1] Martin J. Berg,[1] John F. Smiley,[5] Balapal S. Basavarajappa,[2,4,6,7] and Ralph A. Nixon[1,2,8,9,11,*]

[1]Center for Dementia Research, Nathan Kline Institute for Psychiatric Research, Orangeburg, NY 10962, USA
[2]Department of Psychiatry, New York University Langone Health, New York, NY 10016, USA
[3]Colorado State University, Department of Biomedical Sciences, Fort Collins, CO 80523, USA
[4]Department of Analytical Psychopharmacology, Nathan Kline Institute for Psychiatric Research, Orangeburg, NY 10962, USA
[5]Department of Neurochemistry, Nathan Kline Institute for Psychiatric Research, Orangeburg, NY 10962, USA
[6]New York State Psychiatric Institute, New York, NY 10032, USA
[7]Department of Psychiatry, College of Physicians and Surgeons, Columbia University, New York, NY 10032, USA
[8]Department of Cell Biology, New York University Langone Health, New York, NY 10003, USA
[9]NYU Neuroscience Institute, New York, NY 10003, USA
[10]Cellular and Molecular Biology Training Program, New York University Langone Health, New York, NY 10003, USA
[11]Lead Contact
*Correspondence: ralph.nixon@nki.rfmh.org
https://doi.org/10.1016/j.celrep.2020.108420

SUMMARY

Neuronal endosomal dysfunction, the earliest known pathobiology specific to Alzheimer's disease (AD), is mediated by the aberrant activation of Rab5 triggered by APP-β secretase cleaved C-terminal fragment (APP-βCTF). To distinguish pathophysiological consequences specific to overactivated Rab5 itself, we activate Rab5 independently from APP-βCTF in the PA-Rab5 mouse model. We report that Rab5 overactivation alone recapitulates diverse prodromal and degenerative features of AD. Modest neuron-specific transgenic Rab5 expression inducing hyperactivation of Rab5 comparable to that in AD brain reproduces AD-related Rab5-endosomal enlargement and mistrafficking, hippocampal synaptic plasticity deficits via accelerated AMPAR endocytosis and dendritic spine loss, and tau hyperphosphorylation via activated glycogen synthase kinase-3β. Importantly, Rab5-mediated endosomal dysfunction induces progressive cholinergic neurodegeneration and impairs hippocampal-dependent memory. Aberrant neuronal Rab5-endosome signaling, therefore, drives a pathogenic cascade distinct from β-amyloid-related neurotoxicity, which includes prodromal and neurodegenerative features of AD, and suggests Rab5 overactivation as a potential therapeutic target.

INTRODUCTION

Endosome dysfunction is strongly implicated in the pathogenesis of Alzheimer's disease (AD) based on robust neuropathological, genetic, and biological evidence (Nixon, 2017). Abnormally enlarged early endosomes positive for the small guanosine triphosphatase (GTPase) Rab5 are invariably observed in late-onset AD and early-onset forms of AD due to amyloid precursor protein (APP) mutation or duplication, and are the earliest neuronal pathology specific to this disease thus far identified. Endosome anomalies precede amyloid β (Aβ) deposition in AD and begin to appear perinatally in Down syndrome (DS), the most common cause of early-onset AD (Cataldo et al., 2000, 2004). Endosome enlargement accompanying accelerated endocytosis and fusion (Cataldo et al., 1997, 2008), upregulated transcription of endocytosis-related genes (Ginsberg et al., 2010a, 2010b, 2011), and aberrant signaling by endosomes are the immediate consequences of pathological Rab5 overactivation (Cataldo et al., 2008; Kim et al., 2016; Xu et al., 2016) and can be reversed by normalizing Rab5 activity (Kim et al., 2016; Xu et al., 2016). In DS primary fibroblasts (Jiang et al., 2010; Kim et al., 2016) and neurons of AD and DS models, Rab5 overactivation has been shown to be strictly dependent on APP-βCTF (carboxyl-terminal fragment). In the case of DS (trisomy 21) APP-βCTF is elevated due to an extra copy of APP (Jiang et al., 2010, 2016; Kim et al., 2016; Nixon, 2017) and, in AD, due to increased β-site APP-cleaving enzyme 1 (BACE1) activity (Pera et al., 2013) despite normal APP expression (Kim et al., 2016). APP-βCTF on endosomes directly binds and recruits the signaling molecule APPL1 (adaptor protein containing pleckstrin homology domain, phosphotyrosine binding domain and leucine zipper motif), which

stabilizes the active form of Rab5 (GTP-Rab5) on endosomes (Kim et al., 2016).

APP-βCTF-dependent endosomal enlargement has also been confirmed in neurons from AD patients (Kim et al., 2016). patient-derived human induced pluripotent stem cell (iPSC) (Israel et al., 2012; Hung and Livesey, 2018), and CRISPR-generated iPSC lines carrying familial AD mutations (Kwart et al., 2019), further corroborating Rab5-mediated endosomal dysfunction as a unifying cytopathological hallmark of AD. In addition to APP, other genetic AD risk factors may promote Rab5 activation by APP-βCTF-dependent or -independent mechanisms, including the E4 allele of apolipoprotein E (Cataldo et al., 2000; Liu et al., 2013; Lin et al., 2018) and RIN3 encoding for guanine nucleotide exchange factors (GEFs) catalyzing the guanosine diphosphate (GDP)-to-GTP exchange (Kajiho et al., 2003; Lambert et al., 2013; Xu et al., 2018). Additional genes and proteins associated with increased AD risk or progression (Karch and Goate, 2015; Lambert et al., 2013) contribute to endosome swelling by regulating endosome exit routes (Cormont et al., 2003; Fjorback and Andersen, 2012; Miranda et al., 2018; Young et al., 2015), and others known to regulate lipid carrying functions mediated by endosomes (Karch and Goate, 2015) or endocytosis/trafficking and fusion of synaptic vesicles (Calafate et al., 2016; David et al., 1996; Harel et al., 2008; Zhang et al., 1998) have potential influences on Rab5 activation.

Rab5 mediates a broad range of neuronal signaling functions, as elucidated by *in vitro* studies in which Rab5 is overexpressed at high levels via transfection or viral gene delivery (Brown et al., 2005; Liu et al., 2007; Xu et al., 2016). Although fundamental, these studies provide associations rather than proof of principle that Rab5 participates in these different processes *in vivo*. More importantly, many of these Rab5-regulated functions are also known to be negatively affected at early stages of AD by APP-βCTF/Aβ, such as synaptic plasticity and propagation of growth factor-mediated trophic signaling (Baglietto-Vargas et al., 2018; Bourgeois et al., 2018; Hsieh et al., 2006; Israel et al., 2012; Kim et al., 2016; Shankar et al., 2008; Xu et al., 2016). However, the contribution of endosomal dysfunction induced directly by Rab5 overactivation to these prodromal changes, as opposed to other actions mediated by APP-βCTF/Aβ, is uncertain. In addition, while endosomal abnormalities persist as the disease progresses beyond the prodromal phase, endosomal dysfunction has not been considered as a possible contributor to the neurodegenerative phase that follows, which is instead attributed to Aβ's triggering tau-mediated neuronal degeneration and amyloid plaque deposition (Carrillo et al., 2013; Dubois et al., 2014). As yet, there are no *in vivo* studies modeling endocytic dysfunction itself as a potential driver of early or late AD neuropathology or attempting to distinguish the effects of Rab5 activation from those exerted by APP.

Here, we induced AD-related Rab5 overactivation dissociated from its major APP-βCTF trigger by generating a transgenic mouse overexpressing Rab5 specifically in neurons via a Thy-1 promoter. While bypassing any APP-βCTF elevation, the stimulus in AD mainly responsible for overactivating Rab5, we were able to approximate the Rab5 expression increase and the level of abnormal Rab5 activation that is seen in AD neurons and DS cells while avoiding confounding influences attributable to APP activity/processing. Remarkably, this mouse model reproduced a broad range of AD-related cellular and functional abnormalities known to arise during both the prodromal and neurodegenerative/clinical phases of AD. Thus, once triggered in AD/DS, Rab5 overactivation by itself appears to become a critical driver of AD prodromal pathobiology and neurodegeneration of the key cholinergic neuronal population linked to memory decline (Chen and Mobley, 2019; Granholm et al., 2000; Grothe et al., 2012; Iulita and Cuello, 2016; Jiang et al., 2016; Muth et al., 2010; Salehi et al., 2006) and that is known to be vulnerable to neurodegeneration at the early stages of AD (Grothe et al., 2012; Muth et al., 2010). Until now, the degenerative/clinical phase of AD has been attributed exclusively to the neurotoxic effects of Aβ/β-amyloid. Our results uncover an *in vivo* Aβ-independent Rab5-mediated pathogenic process beginning at the earliest prodromal stage of AD and leading to degeneration within a neuronal circuit vulnerable at early AD stages and critically involved in cognition. This pathogenic process advances in parallel to the additional neurotoxic events initiated by Aβ/β-amyloid. Moreover, Rab5 overactivation and its signaling effectors are potential targets for therapeutic interventions against AD.

RESULTS

Direct Neuronal Rab5 Overactivation *In Vivo* Reproduces AD-Related Endosomal Dysfunction

An ~1.5-fold upregulation of Rab5 expression in AD (Ginsberg et al., 2010b) and DS (Cataldo et al., 2008) results in accelerated endocytosis and increased endosome fusion due to APP-βCTF-mediated Rab5 overactivation (Jiang et al., 2010; Kim et al., 2016; Xu et al., 2016). To isolate the role of pathological activation of Rab5 *in vivo* from APP-βCTF, we generated transgenic mice, hereafter named PA-Rab5, overexpressing myc-tagged human Rab5a specifically in neurons via a Thy-1 promoter, which directs widespread neuronal transgene expression postnatally (Barlow and Huntley, 2000).

We measured Rab5a expression levels in cortical or hippocampal homogenates (Figures 1A and S1A) between 3 and 15 months of age by western blot analysis. Rab5 expression (endogenous+myc-Rab5a transgene) was moderately increased in PA-Rab5 mice, being ~2.5-fold higher, compared to wild-type (WT) littermates (Figure 1B), as observed in AD (Ginsberg et al., 2010b) and DS (Cataldo et al., 2008). A similar, although slightly lower, increase in Rab5 was observed in cortical homogenates probed with a pan-Rab5 antibody (Figure S1B), which is consistent with the specific overexpression of Rab5a (see respective figure legend and STAR Methods for further details). Myc-Rab5a transgene, as detected by a myc-tag-directed antibody, was only seen in PA-Rab5, running between 25 and 30 kDa, as expected (Figures S1A and S1B).

Anti-Myc and -Rab5 immunofluorescence (IF) for regional evaluation of Rab5 expression (Figure S1C) revealed the highest transgene expression in the cortex, hippocampus, amygdala, and midbrain and lower expression in the thalamus, striatum, and cerebellum.

This moderate increase in Rab5 expression resulted in a significant overactivation of Rab5 in both hippocampal (Figures 1C, 1D, S1D, and S1E) and cortical (Figures 1E, 1F, S1E, and S1F)

CellPress
OPEN ACCESS

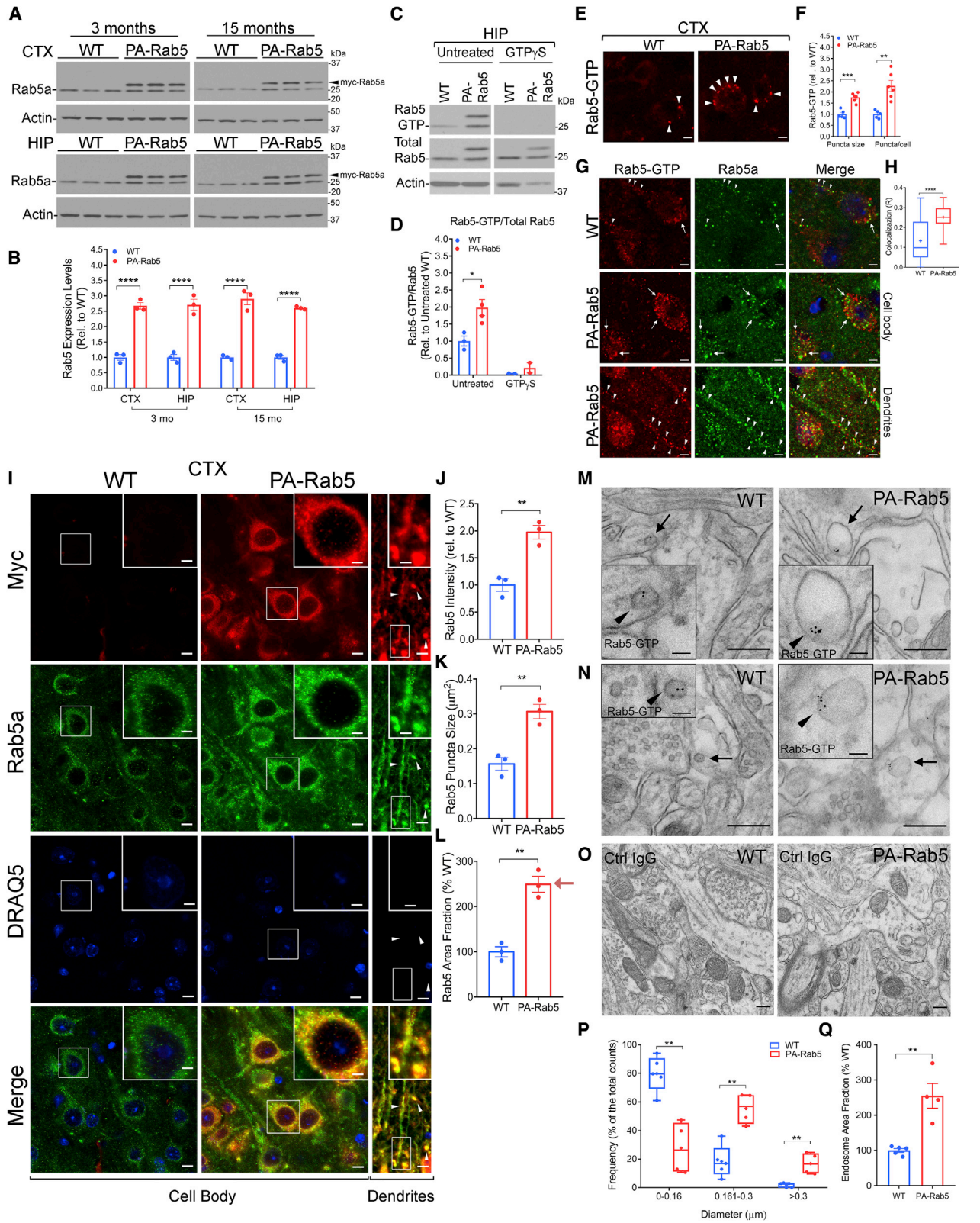

(legend on next page)

samples of 6- to 8-month-old PA-Rab5 compared with WT littermates, as assessed by multiple approaches. The levels of activated, GTP-bound Rab5 in hippocampal homogenates were determined by a GTP-agarose pull-down assay (Xu et al., 2016), followed by detection with anti-Rab5 antibody (Figure 1C). We determined an ~2-fold increase in GTP-bound Rab5 (expressed as Rab5-GTP/total Rab5) in PA-Rab5 mice compared with WT (Figure 1D). A separate reaction in the presence of GTPγS, a non-hydrolyzable GTP analog, before sample incubation with GTP-agarose beads was carried out that demonstrated low binding. Then, we directly measured levels of activated Rab5 in hippocampal endosome-enriched cytosolic (EEcyt) preparations by selective immunoprecipitation (IP) with a Rab5-GTP-specific antibody (Figure S1D). Immunoblot analysis confirmed Rab5 overactivation in PA-Rab5 mice, as shown by greater IP of GTP-bound Rab5, compared to WT mice. As an additional approach, we performed IP of the Rab5 GEF, RabGEF-1, from EEcyt (Figure S1E), followed by detection with both RabGEF-1 and Rab5. Our results demonstrated increased IP of RabGEF-1, both alone and in complex with Rab5, in PA-Rab5 mice compared to WT mice (Figure S1E). Of importance, similar results were obtained in the GTPγS-treated condition, thus supporting Rab5 overactivation in PA-Rab5 mice. Furthermore, separation of endosome-enriched (EE) from cytosolic (Cyt) and other non-endosomal compartments by iso-osmotic density flotation gradient of cortical post-nuclear supernatants (PNSs) (Figure S1F) showed co-fractionation of both RabGEF-1 and Rabaptin5, with Rab5 in a representative gradient from a WT mouse. Western blot analysis of isolated pooled EE and Cyt fractions revealed a significant increase in EE levels of Rab5 and Rabaptin-5 in PA-Rab5, compared to WT (Figure S1G). Collectively, these biochemical and functional assays provide compelling evidence of Rab5 overactivation and increased endosomal effector recruitment in PA-Rab5 mice, compared to WT mice, as previously shown *in vitro* (Christoforidis and Zerial, 2000; Lippé et al., 2001; Stenmark et al., 1995; Zhang et al., 2014; Zhu et al., 2007). Finally, *in situ* IF labeling with the Rab5-GTP specific antibody (Figure 1E) revealed increased numbers and size of Rab5-GTP$^+$ puncta per cell in PA-Rab5 pyramidal cortical neurons (Figure 1F), as compared to WT mice. Rab5-GTP$^+$ puncta colocalized with Rab5a endosomes both in cell bodies (Figure 1G, arrows) and dendrites (Figure 1G, arrowheads) in double IF staining. This colocalization was significantly increased in PA-Rab5, compared to WT (Figure 1H). The proportion of CA1 pyramidal neurons covered by Rab5-GTP$^+$ puncta was also significantly increased in PA-Rab5, compared to WT (data not shown). Notably, increased Rab5 expression/activation did not alter APP metabolite levels, as detected by western blot analysis using C1/6.1 antibody (Figure S1H) or by ELISA analysis of mouse Aβ40, Aβ42, and relative Aβ42/Aβ40 ratio (Figure S1I), indicating a negligible downstream effect of Rab5 overactivation on APP processing.

We next carried out morphological analyses of Rab5 endosomes by IF labeling of tissue sections using anti-Myc and -Rab5 antibodies (Figure 1I). Myc-Rab5 transgene was detected in the cell body (Figure 1I, inset) and dendrites of PA-Rab5 cortical neurons (Figure 1I, arrowheads), which showed Rab5$^+$ puncta to have an ~2-fold increased IF intensity, size, and proportion of total cell area covered, compared with WT mice (Figures 1J–1L), in accordance with expected Rab5-GTP-mediated enhancement of homotypic Rab5-endosome fusion (Gorvel et al., 1991) and as seen in AD and DS (Jiang et al., 2010; Kim et al., 2016) (Figure 1L, arrow). PA-Rab5 CA1 pyramidal neuron cell bodies (Figure S1J) and dendrites (Figure S1F, arrowheads and respective inset) also showed similar changes in Rab5$^+$ puncta IF intensity, size, and proportion of total endosomal area (Figure S1K). PA-Rab5 endosome identity was further confirmed by post-embedding immunogold electron microscopy (EM) with antibodies

Figure 1. Direct Neuronal Rab5 Overactivation *In Vivo* Reproduces AD-Related Endosomal Dysfunction

(A and B) Representative western blots (A) and quantification (B) of Rab5a expression in WT and PA-Rab5 cortical (CTX) and hippocampal (HIP) homogenates at 3 and 15 months, as detected by a Rab5a antibody and enhanced chemiluminescence (ECL) with film exposure within the linear range of the signal. Both endogenous and myc-Rab5a transgene (arrowhead) were detected (1-way ANOVA with Sidak's post hoc test; n = 3 mice/genotype/brain region/age group). See also Figures S1A and S1B.

(C and D) Representative western blots (C) and quantification (D) of Rab5 activation in 6-month-old WT and PA-Rab5 HIP by GTP-agarose pull-down and detection with a Rab5a antibody. Rab5 activation is expressed as Rab5-GTP/total Rab5. Pre-treatment with GTPγ-S before pull-down served as negative control. Data normalized to the untreated WT control group (1-way ANOVA with Dunnett's post hoc test; untreated WT n = 3, PA-Rab5 n = 4; GTPγ-S-treated WT n = 2, PA-Rab5 n = 2). See also Figures S1D–S1G.

(E and F) Representative confocal images (E) and quantification (F) of activated Rab5 in the CTX at 7 months. Rab5-GTP puncta (arrowheads) size and number per cell are increased in PA-Rab5, compared to WT (WT n = 5; PA-Rab5 n = 6). Scale bars, 5 μm.

(G) Representative confocal images of WT and PA-Rab5 cortical neurons displaying Rab5-GTP (red) and anti-Rab5a (green) localization in the cell body (arrows) and dendrites (arrowheads). Cell nuclei were counterstained with DRAQ5 (blue). Scale bars, 5 μm.

(H) Colocalization analysis (R) of Rab5-GTP and Rab5a by Pearson's correlation coefficient (R: WT = 0.124 ± 0.02 PA-Rab5 = 0.252 ± 0.01; n = 30 cells/genotype).

(I) Representative confocal images of cortical neurons from 7-month-old WT and PA-Rab5 tissue sections double-labeled with anti-Myc (red) and anti-Rab5a (green) antibodies. Cell nuclei were counterstained with DRAQ5 (blue). Myc-Rab5 is detected in the cell body (insets) and dendrites (arrowheads and respective insets) of PA-Rab5. In the insets, the brightness/contrast of the red channel was equally adjusted to better visualize Myc-Rab5 soluble and membrane-bound pools. To better visualize dendritic Myc-Rab5, the laser intensities for the red and green channels were enhanced. Scale bars, 5 μm; insets, 2.5 μm.

(J–L) Quantification of Rab5a$^+$ vesicle intensity (J), size (K), and proportion of cell area covered (L). The arrow in (L) indicates the levels of Rab5 total endosome area previously observed in AD and DS, for comparison (n = 3 mice/genotype).

(M–O) Post-embedding immunogold EM identified enlarged Rab5-GTP$^+$ vesicles (arrows and arrowheads in respective insets) in neurites (M) and post-synaptic terminals (N) of PA-Rab5 prefrontal cortex (PFC) layer V, compared to WT. (O) No gold particles were detected in samples incubated with mouse immunoglobulin G (IgG) isotype control. Scale bars, 250 nm; inset, 50 nm. See also Figure S1H.

(P and Q) Ultrastructural EM analysis of endosome size distributions (P) and endosome area fraction (Q) performed on images taken from PFC layer V (WT n = 5, PA-Rab5 n = 4).

*p < 0.05; **p < 0.01; ***p < 0.001; ****p < 0.0001; 2-tailed Student's t test unless otherwise specified. Data are means ± SEMs.

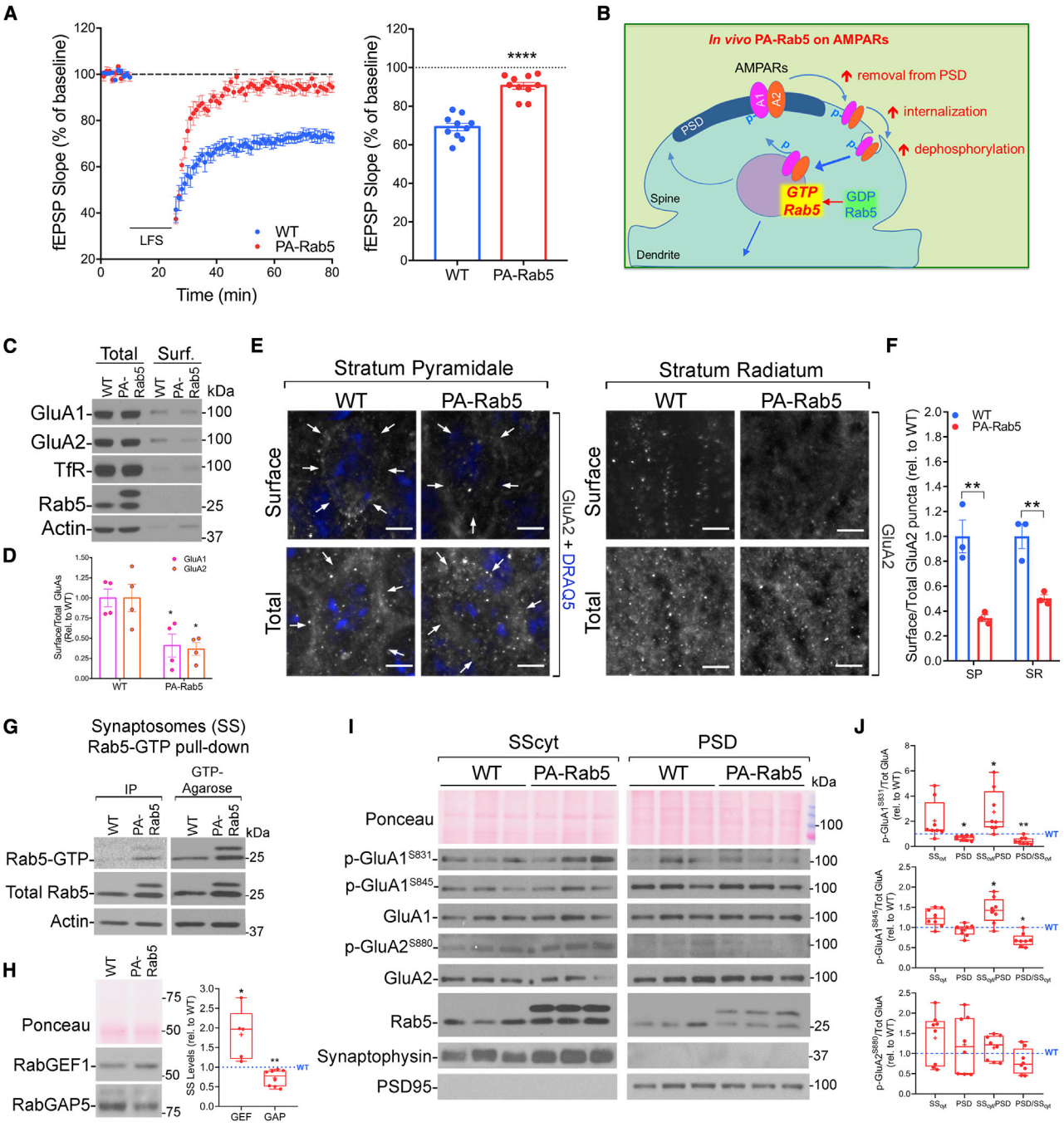

Figure 2. Pathological Rab5 Activation in PA-Rab5 Mice Disrupts Hippocampal LTD and Accelerates AMPAR Endocytosis

(A) LTD induced by low-frequency stimulation (LFS) is defective in PA-Rab5 mice at 6 months. The fEPSP slopes were normalized to the average value 10 min before LFS stimulation. A combined plot of the averages of fEPSP slopes at 50 min shows the absence of LTD induced by LFS in PA-Rab5 compared with WT mice (n = 10 slices from n = 8 mice/genotype).

(B) Rab5 overactivation drives the removal of AMPARs from synapses and promotes internalization associated with GluA1 subunit dephosphorylation.

(C and D) Representative western blots (C) and quantification (D) of the relative surface/total levels of GluA1 and GluA2 receptors following surface biotinylation of 6.5-month-old mouse acute hippocampal slices, normalized to WT slices (n = 4 independent labeling reactions/genotype, n = 2 mice/genotype; n = 8–10 slices/reaction). See also Figures S2A and S2B.

(E) Representative confocal images of GluA2 IF in CA1 pyramidal neurons (stratum pyramidale [SP], arrows) and dendrites (stratum radiatum [SR]) in 7-month-old mice. Cell surface GluA2 receptors were labeled under non-permeant conditions (Surface); the total population was probed under permeant conditions (Total). Cell nuclei were counterstained with DRAQ5 (blue). Scale bars, 5 μm. See also Figure S2C.

(legend continued on next page)

against GTP-Rab5, which specifically recognized enlarged endosomes (Figure S1L) in PA-Rab5 neurites (Figure 1M) and post-synaptic terminals (Figure 1N), total Rab5, and the endosomal Na^+/H^+ exchanger NHE6 (Figure 1M). Negligible staining was observed in the absence of specific primary antisera (Figure 1O and bottom panels in Figures S1L and S1M). EM ultrastructural characterization of endosomes, identified as vesicles with single limiting membranes and sparse intraluminal content (Gruenberg et al., 1989), showed that PA-Rab5 mice had a significantly reduced frequency of endosomes with diameter <160 nm, paralleled by a significant increase in numbers of endosomes with diameters >160 nm (Figure 1P), resulting in a 2.5-fold higher total endosomal area as compared with WT mice (Figure 1Q), similar to the IF results (Figure 1L).

These results show that a moderate increase in Rab5 expression is sufficient to drive significant overactivation of Rab5 *in vivo* comparable in degree to that observed in AD (Cataldo et al., 2008; Ginsberg et al., 2010b; Kim et al., 2016), resulting in an AD-like endosome phenotype, in the absence of an elevation of APP metabolite levels.

Pathological Rab5 Activation *In Vivo* (PA-Rab5) Impairs Long-Term Depression (LTD) by Accelerating Synaptic α-Amino-3-hydroxy-5-methyl-4-isoxazolepropionic Acid Receptor (AMPAR) Internalization

Next, we sought to determine the effect of Rab5 over-activation *in vivo* on the physiological control of synaptic plasticity, given the role of Rab5 in LTD formation via AMPAR endocytosis (Hausser and Schlett, 2019), which is also affected by APP-βCTF/Aβ (Hsieh et al., 2006; Shankar et al., 2008). Functionally, Rab5 overactivation in 6-month-old PA-Rab5 mice significantly suppressed LTD upon induction by low-frequency stimulation (LFS) (1 Hz for 900 s) at hippocampal Schaffer collateral-CA1 synapses (Figure 2A), whereas LTD was efficiently induced in WT slices, as shown by a significant lasting decrease in field excitatory post-synaptic potential (fEPSP) slope.

As summarized in Figure 2B, overactivation of Rab5 drives the removal of AMPARs from the post-synaptic surface, followed by receptor internalization via endocytosis. This process, which occurs during hippocampal LTD, has been shown to be associated with changes in the phosphorylation of the GluA1 AMPAR subunit at specific sites (Lee et al., 2000) and has so far been reproduced only by *in vitro* overexpression of Rab5 (Brown et al., 2005). Therefore, we addressed the biochemical basis of Rab5-mediated suppression of LTD *in vivo*. Surface biotinylation of acute hippocampal slices from PA-Rab5 revealed a significant reduction in the surface/total ratio of GluA1 and GluA2 AMPAR subunits, compared to WT slices (Figures 2C and 2D), despite similar total receptor levels (Figures S2A and S2B), suggesting increased AMPAR endocytosis.

We further determined the cellular localization of AMPARs *in situ* by IF labeling with an antibody against the extracellular domain of GluA2 (Figure 2E), thus allowing us to distinguish between surface and total receptors under non-permeant and permeant conditions. $GluA2^+$ puncta, reflecting receptor clustering at synapses, were visualized in CA1 stratum pyramidale and stratum radiatum (Figures 2E and S2C). Our results show that few surface puncta were observed in PA-Rab5, compared to WT, suggesting that the vast majority of total GluA2 immunoreactivity represented non-surface receptors. This was confirmed by a significant reduction in the relative ratio of surface:total GluA2 puncta in both regions in PA-Rab5, compared to WT (Figure 2F), despite similar proportions of total GluA2 puncta (Figure S2D). Similarly, $GluA1^+$ puncta at the surface (Figure S2E) and GluA1surface:total ratios (Figure S2F) were reduced in PA-Rab5, relative to WT, with comparable proportions of total GluA1 puncta.

To determine whether Rab5-mediated reduction in the levels of surface AMPARs was accompanied by changes in AMPAR phosphorylation, we used synaptosomal preparations isolated from WT and PA-Rab5 hippocampi. We determined increased levels of Rab5 activation in 6-month-old PA-Rab5 mouse synaptosomes (SSs), compared with WT, by both IP with the Rab5-GTP specific antibody and by GTP-agarose pull-down of Rab5-GTP (Figures 2G and S2G). Also, the synaptosomal levels of the Rab5 effector Rab-GEF-1 (Horiuchi et al., 1997) and those of the GTPase-activating protein RabGAP5 were increased and decreased, respectively, in PA-Rab5, compared to WT, reflecting Rab5 overactivation (Figure 2H). Further extraction of total SS into SS soluble/cytosolic (SScyt) and post-synaptic density (PSD)/membrane fractions (Figures 2I and S2H) revealed a significant increase in the ratio of soluble:membrane (SScyt:PSD), or conversely, a significant decrease in the ratio of membrane:soluble (PSD:SScyt), for p-$GluA1^{S831}$ and p-$GluA1^{S845}$ in PA-Rab5 (Figures 2I and 2J), compared to WT mice, consistent with AMPAR removal from the PSD membrane and internalization by endocytosis (Brown et al., 2005). Rab5 overactivation *in vivo* did not alter the phosphorylation of p-$GluA2^{S880}$, as previously shown for *in vitro* Rab5 overexpression in organotypic slices (Brown et al., 2005). With respect to the initial homogenates, GluA1 and GluA2 were significantly enriched in SS and PSD fractions, and their levels were similar between WT and PA-Rab5 mice (Figures S2H and S2I).

These results indicate that overactivated Rab5 *in vivo* promotes the removal from the surface and accelerates the

(F) Quantification of the surface:total $GluA2^+$ puncta ratio relative to WT shows a significant decrease in PA-Rab5 in SP and SR (n = 3 mice/genotype). See also Figures S2C and S2D.

(G) Representative western blots of Rab5-GTP pulled down from 6-month-old WT and PA-Rab5 hippocampal synaptosomes (SS) by immunoprecipitation (IP) and GTP-agarose beads, followed by detection with Rab5a. Experiments were repeated twice, with similar results. See also Figure S2G.

(H) Representative western blots and quantification of RabGEF-1 and RabGAP5 levels in hippocampal SS of PA-Rab5 mice, relative to WT (dotted line) (n = 5–8 mice/genotype).

(I) Representative western blot showing the distribution of p-$GluA1^{S831}$, p-$GluA1^{S845}$, and p-$GluA2^{S880}$, and respective non-phosphorylated forms, in SS soluble/cytosol (SScyt) and post-synaptic density (PSD)/membrane fractions, extracted from hippocampal SS of 8.5 month-old mice.

(J) Quantification of the 3 phospho-AMPAR:total AMPAR ratios in SScyt and PSD fractions, and respective SScyt:PSD or PSD:SScyt ratios, relative to WT (dotted line) (n = 8 mice/genotype).

*p < 0.05; **p < 0.01; ***p < 0.001; 2-tailed Student's t test. Data are means ± SEMs.

endocytosis of the same pool of AMPARs that are affected during LTD, thus mimicking and occluding LTD induced by LFS (Figure 2A).

PA-Rab5 Mice Exhibit Long-Term Potentiation (LTP) Deficits and Hippocampal Spine Abnormalities

Input/output responses of fEPSPs evoked by increasing the stimulation of the CA1-Schaffer collateral pathway were comparable between WT and PA-Rab5 hippocampal slices at 6 months (Figure 3A). However, PA-Rab5 mice showed a significant impairment in LTP following theta-burst stimulation (TBS) at Schaffer collateral-CA1 synapses, compared with WT mice (Figure 3B). These findings strongly suggest that Rab5 overactivation *in vivo* negatively influences CA1 hippocampal synaptic plasticity without, however, altering basal neurotransmission.

To address whether PA-Rab5 functional deficits in synaptic plasticity altered dendritic spines, we used a rapid Golgi impregnation method to analyze hippocampal CA1, CA3 pyramidal neuron, and dentate gyrus (DG) granule cell spines in 8.5-month-old mice (Figure 3C). Compared with WT, PA-Rab5 mice displayed a significant reduction in spine density in CA3 and DG (Figure 3D), but not in the CA1 region. Cumulative distribution curves of CA1 spine length revealed a shift toward smaller sizes in PA-Rab5 relative to WT (Figure 3E), comparable in degree to that observed in age-matched 5XFAD mice (Figure S3A), an aggressive model of AD that develops marked synaptic and neuronal loss (Eimer and Vassar, 2013; Oakley et al., 2006). A similar shift was also observed in the PA-Rab5 CA3 region, but not in the DG (Figures S3B and S3C). Accordingly, the overall average length of CA1 and CA3 neuron dendritic spines was significantly lowered (Figure 3F). In addition, as evidenced by ultrastructural analysis of CA1 dendritic spines, PA-Rab5 showed a higher frequency of short "stubby" spines (~71.4%), without a well-defined neck or lacking constriction between the head and shaft (Tackenberg et al., 2009), compared to non-stubby spines (~28.6%); WT mice exhibited reversed proportions (~23.8% stubby and ~76.2% non-stubby) (Figures 3G and 3H). Similar changes in dendritic spine morphology have been observed in human AD brain (Androuin et al., 2018) and mouse models of DS (Belichenko et al., 2004; Haas et al., 2013) and were shown to correlate with LTP impairment in a mouse model of AD (Androuin et al., 2018). These findings indicate that Rab5-mediated impairment in LTP is also accompanied by morphological changes and loss of hippocampal dendritic spines.

PA-Rab5 Mice Exhibit Abnormal AKT Signaling and Tau Hyperphosphorylation via Overactivated Glycogen Synthase Kinase-3β (GSK-3β)

Pro-survival neurotrophin signaling, occurring via the tyrosine-kinase phosphatidylinositol-3-kinase (PI3K)/AKT pathway, which depends on Rab5-regulated endocytosis and early endosome transport (Goto-Silva et al., 2019), is defective in AD (Chen et al., 2018). Moreover, pathological activation of GSK-3β, a kinase downstream of AKT (Hooper et al., 2008) contributing to tau hyperphosphorylation, has been linked to sporadic and familial AD (Hooper et al., 2008; Israel et al., 2012). To determine the effect of neuronal pathological activation of Rab5 *in vivo* on the AKT/GSK-3β pathway, we performed western blot analysis on cortical homogenates of 15-month-old mice (Figures 4A and 4B). We found that PA-Rab5 showed a significant decrease in the phosphorylation of AKT, both absolute and relative to total AKT levels, on threonine 308 (p-AKT^{T308}) and serine 473 (p-AKT^{S473}), compared with WT, indicating the downregulation of AKT activity, which is consistent with reduced growth factor-mediated trophic support (Dou et al., 2013). Dysregulation of AKT signaling in PA-Rab5 mice may also result from the increased endocytosis of growth factor/receptor complexes from the plasma membrane due to overactivated Rab5 and/or abnormal recruitment of effectors on enlarged endosomes (Chen et al., 2018) and consequent displacement from their normal targets/functions (Dou et al., 2013). AKT activation was also significantly reduced in PA-Rab5 hippocampal homogenates (Figure S4A). PA-Rab5 mice also showed a significantly decreased phosphorylation of GSK-3β on serine 9 (p-GSK-3β^{S9}), the inactive form and substrate of p-AKT^{S473}, and conversely, significantly increased levels of constitutively active GSK-3β phosphorylated on tyrosine 216 (p-GSK-3β^{Y216}) (Figures 4C and 4D), compared to WT, in accordance with increased GSK-3β activity. GSK-3β^{Y216}/total GSK-3β was also significantly elevated in PA-Rab5 hippocampal homogenates (Figure S4B). Double IF staining with p-GSK-3β^{S9} and Rab5-GTP antibodies of 15-month-old mouse tissue sections (Figure 4E) further confirmed a significantly reduced p-GSK-3β^{S9} IF intensity, indicating greater GSK-3β activation, in cortical layer II/III neurons of PA-Rab5 compared to WT, which was accompanied by significant Rab5 overactivation, as measured by the increased numbers and size of Rab5-GTP^{+} puncta per cell (Figure 4F).

As a readout of GSK-3β activity, we monitored changes in tau phosphorylation at GSK-3β-directed sites (Tenreiro et al., 2014) using Paired Helical Filament 1$^{S396/404}$ (PHF-1$^{S396/404}$) and CP13^{S202} antibodies. It is important to note that these epitopes are associated with tauopathy within affected subpopulations of neurons during the earliest stages of AD and DS (Mondragón-Rodríguez et al., 2014). Perikaryal PHF-1 immunoreactivity in PA-Rab5 was increased selectively across neuronal populations in layers II/III and V (Figure 4G), as confirmed by semiquantitative analysis (Figure 4H). Within these laminae of cortex, further analyses carried out using a WT-based intensity threshold (as per STAR Methods) confirmed the PHF-1 increase, compared to WT (Figure 4I, top graph in 4J). By contrast, CP13 immunoreactivity was elevated selectively in layer II/III neurons and involved only ~50% of this population, as determined by semiquantitative analysis (total counts: WT n = 98 neurons; PA-Rab5 n = 168 neurons) (Figure 4I, bottom graph 4J, arrows). Because of this cell and regional selectivity of tau hyperphosphorylation within tissues that otherwise contained a higher proportion of normally phosphorylated tau, western blot analysis could not discriminate the CP13/PHF1 elevations visible by IF (data not shown). By contrast, total tau immunoreactivity in cortical neuron perikarya was significantly and uniformly increased across the cortex in PA-Rab5, compared to WT (Figure S4C), and similar increases were also detected in whole cortical homogenates by western blot analysis (Figure S4D). Layer II/III cortical neurons of PA-Rab5 displayed PHF-1 colocalization

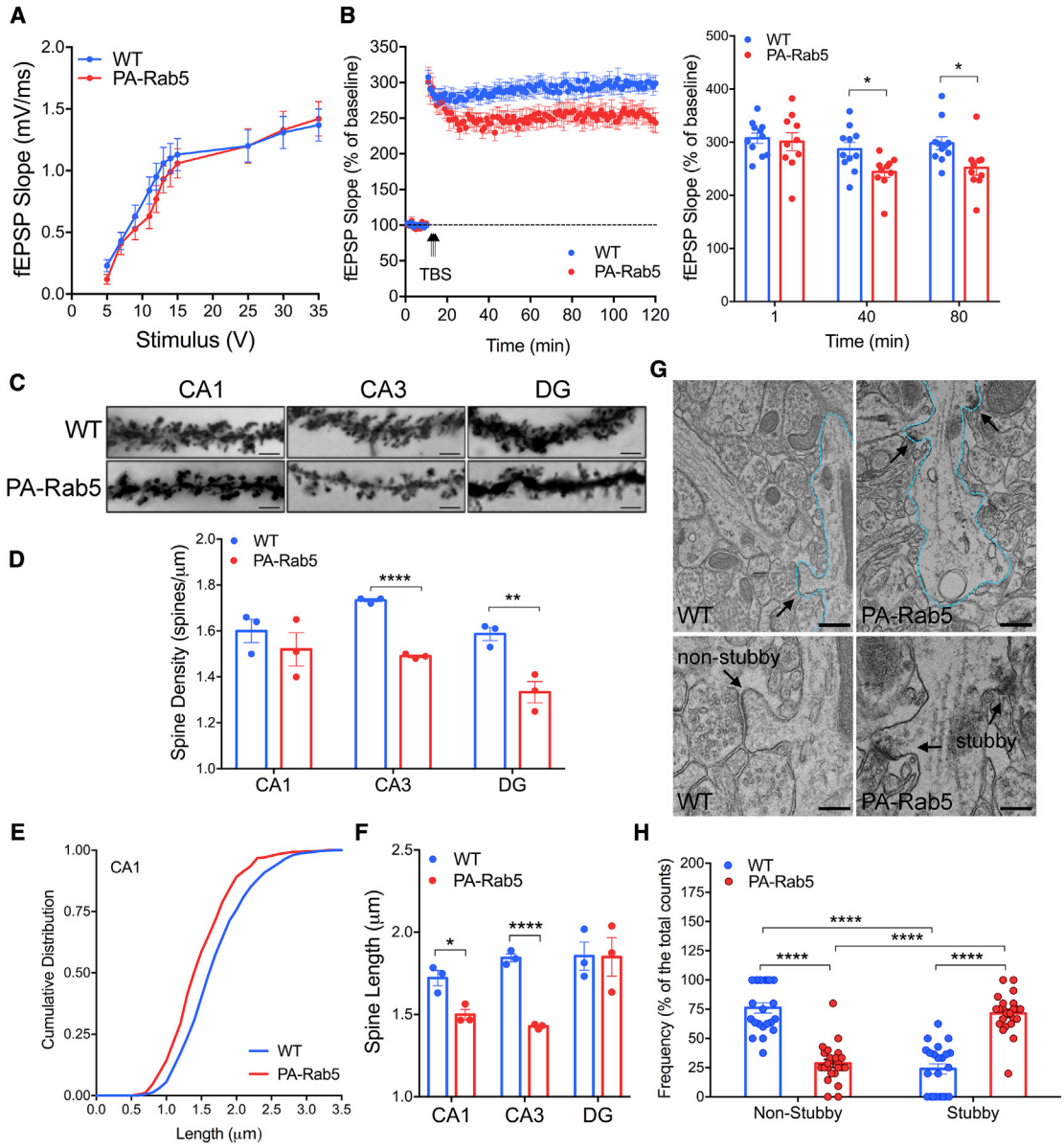

Figure 3. PA-Rab5 Mice Exhibit LTP Deficits and Hippocampal Spine Abnormalities

(A) Input/output relationship plots of hippocampal slices from 6-month-old PA-Rab5 and WT littermates (n = 20 slices from n = 8 mice/genotype).

(B) LTP induced by theta-burst stimulation (TBS) is impaired in PA-Rab5 mice. The fEPSP slopes were normalized to the average value 10 min before stimulation in each experiment. A combined plot of the averages of fEPSP slopes at 1, 40, and 80 min following tetanic stimulation showed a significant decrease in PA-Rab5 as compared with WT mice (1-way ANOVA with Holm-Sidak's post hoc test: WT n = 11 slices, PA-Rab5 n = 10 slices from n = 8 mice/genotype).

(C) Representative photomicrographs of hippocampal CA1, CA3, and dentate gyrus (DG) dendritic segments from 8.5-month-old WT and PA-Rab5 mice. Dendritic spines were sampled on 3–4 dendrites in the dorsal hippocampus per neuron (n = 3 neurons from n = 3 mice/genotype). Scale bars, 2.5 μm.

(D) The average dendritic spine density (spines/μm) is significantly reduced in PA-Rab5 CA3 and DG regions, compared to WT (n = 3 mice/genotype)

(E) Cumulative distribution analysis of CA1 spine lengths shows a shift toward smaller sizes in PA-Rab5, compared to WT (n = 3 mice/genotype; spine counts WT n = 592; PA-Rab5 n = 441).

(F) The average length of dendritic spines is significantly reduced in CA1 and CA3 regions of PA-Rab5, compared to WT (n = 3 mice/genotype).

(G) Representative EM images of CA1 dendrites (upper images, blue-dotted lines) and dendritic spines (arrows) in the SR of 7-month-old WT and PA-Rab5 mice. Scale bars, 0.5 μm. Higher-magnification images (lower panel, arrows) identify non-stubby and stubby spine morphologies in WT and PA-Rab5 mice, respectively. Scale bars, 0.25 μm.

(H) EM image quantification of non-stubby and stubby spine frequencies in WT and PA-Rab5 CA1 SR. Values are expressed as percentage of the total spine counts per image per genotype (1-way ANOVA with Sidak's post hoc test; n = 2 mice/genotype; WT n = 127 spines from n = 22 images; PA-Rab5 n = 149 spines from n = 23 images).

*p < 0.05; **p < 0.01; ***p < 0.001; ****p < 0.0001; 2-tailed Student's t test unless otherwise specified. Data are means ± SEMs.

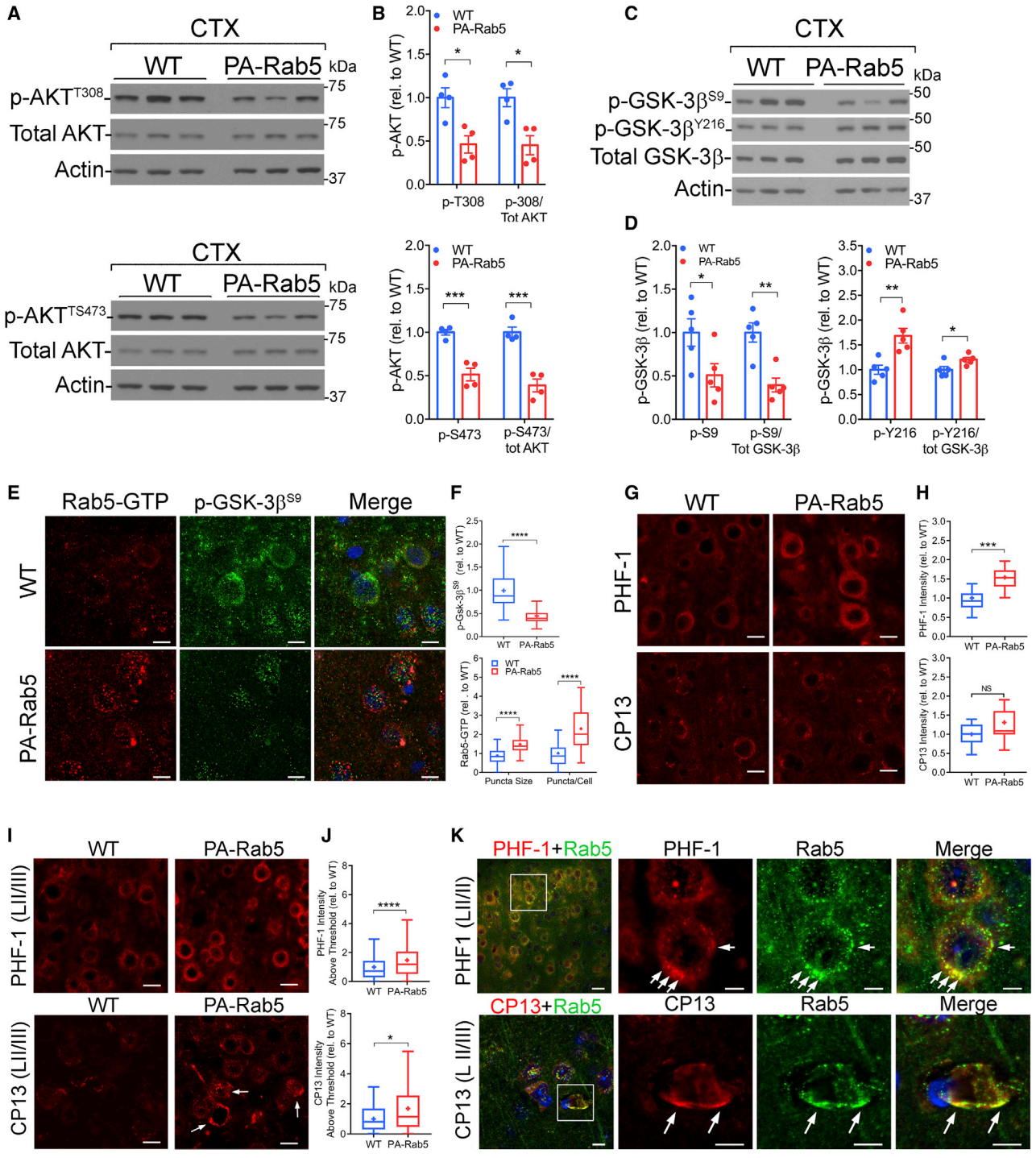

Figure 4. PA-Rab5 Mice Exhibit Abnormal AKT Signaling and Tau Hyperphosphorylation via Overactivated GSK-3β

(A and B) Representative western blots (A) and quantification (B) of p-AKT^{T308} and p-AKT^{S473} in 15-month-old mouse cortical homogenates. AKT phosphorylation, absolute (p-AKT/actin) and relative to total AKT (p-AKT/total AKT), is significantly decreased in PA-Rab5, compared to WT (n = 4 mice/genotype).

(C and D) Representative western blots (C) and quantification (D) of p-GSK-3β^{S9} and p-GSK-3β^{Y216} in 15-month-old mouse cortical homogenates. GSK-3β phosphorylation at both sites, absolute (p-GSK-3β/actin) and relative to total GSK-3β (p-GSK-3β/total GSK-3β), reflects increased activation in PA-Rab5, compared to WT (n = 5 mice/genotype).

(E and F) Representative confocal images (E) and quantification (F) of Rab5-GTP (red) and p-GSK-3β^{S9} (green) in 15-month-old mouse layer II/III cortical neurons. Cell nuclei were counterstained with DRAQ5 (blue). Scale bars, 10 μm. (F) PA-Rab5 showed a significant reduction in the fluorescence intensity of p-GSK-3β^{S9}, and a significant increase in Rab5-GTP puncta size and number of puncta per cell, compared to WT (n = 70 neurons/genotype).

(legend continued on next page)

with Rab5 endosomes in double IF staining (Figure 4K, top panels, arrows). Subsets of neurons from the same region double-labeled with CP13 and Rab5 showed similar p-tau and Rab5 colocalization and revealed an abnormal morphology (Figure 4K, bottom panels, arrow). These results support a role for Rab5 overactivation and endocytic dysfunction in mediating the downregulation of the pro-survival AKT signaling pathway, resulting in increased GSK-3β activation and tau hyperphosphorylation.

In Vivo Rab5 Overactivation Induces Basal Forebrain Cholinergic Neurodegeneration, Hippocampal Abnormalities, and Memory Impairment

The selective loss of basal forebrain cholinergic neurons (BFCNs) caused by aberrant axonal transport and signaling from trophic factors is an early pathological hallmark of AD and DS induced by APP-βCTF-mediated endosome enlargement (Jiang et al., 2016; Kim et al., 2016; Xu et al., 2016) associated with cognitive decline (Granholm et al., 2000; Muth et al., 2010) (Figure 5A). To determine the specific contribution of Rab5 over-activation to BFCN degeneration, we performed choline acetyltransferase (ChAT) immunolabeling of the medial septal nucleus (MSN) BFCNs at different ages. Stereological counting of MSN-ChAT neurons demonstrated a significant aging-dependent loss of BFCNs in PA-Rab5, compared with age-matched WT littermates, starting at 7 months (Figure 5B). Morphological analysis revealed frequent swollen/bead-like profiles (Figure 5C, upper panel, arrowheads) and remarkable dystrophy (Figure 5C, lower panel, arrowheads) of $ChAT^+$ fibers in PA-Rab5 mice as early as 7 months. Furthermore, many PA-Rab5 $ChAT^+$ BFCNs showed abnormal swelling and thickening of proximal dendrites and dysmorphic cell bodies (Figure 5D, arrows). Similar changes have been observed during brain aging and commonly in AD (Nyakas et al., 2011). Double-labeled with anti-ChAT and anti-Myc antibodies (Figure 5E), these abnormal BFCNs accumulated Rab5-immunoreactive puncta at proximal dendrites (Figure 5E, arrow and inset) and showed abnormal bulging of the cell bodies (Figure 5F, arrow), which also accumulated Rab5 puncta, as detected by ChAT and Rab5a double IF labeling (Figure 5G, arrow). These results suggest that Rab5-mediated endosome enlargement, by causing trafficking defects, may also interfere with the axonal transport of ChAT. These results indicate that sustained Rab5 activation *in vivo* is sufficient to cause the degeneration and age-dependent loss of vulnerable BFCNs, thus recapitulating another early feature of AD pathobiology.

MSN-originating BFCNs send their projections primarily to the hippocampus (Ballinger et al., 2016) and rely on the retrograde transport of signaling endosomes from these sites for their survival (Chen and Mobley, 2019). To gain ultrastructural insights into the extent of endosomal pathology in the hippocampus of PA-Rab5 mice, we characterized the CA1 and DG areas of 7-month-old mice by EM (Figure 5H). Compared to WT endosomes (Figure 5H, white arrowheads), PA-Rab5 mice showed an abnormal accumulation of endosomes (Figure 5H, PA-Rab5, white arrowheads) in the dendrites of both CA1 and DG areas. PA-Rab5 mice also displayed mild degenerative profiles, consisting of the presence of autophagic structures in dendrites, pre-synaptic terminals, and neurites (Figure 5H, PA-Rab5, red arrows). These results suggest that defective retrograde transport of signaling endosomes along cholinergic projections in MSN to the hippocampus, together with downregulated AKT-mediated pro-survival signaling (Figure S4A), contribute to the degeneration of BFCNs in PA-Rab5 mice. Furthermore, the hippocampal degenerative phenotype can result directly from Rab5 overactivation in this region or be secondary to the lack of appropriate cholinergic input from the MSN (Haam and Yakel, 2017).

Memory function was examined in 6-month-old mice by the non-spatial hippocampal-dependent novel object recognition test (ORT) (Figure 5I). WT and PA-Rab5 mice showed similar total exploration times during the training (e1) or at 24-h testing (e2) (Figure 5J), however, PA-Rab5 mice showed significantly reduced ORT performance at 24 h retention (Figure 5K) indicating that Rab5 overactivation *in vivo* is sufficient to drive impairment of long-term memory.

DISCUSSION

The formulation of a preclinical or prodromal stage of AD highlights the concept that AD starts silently decades before the diagnostic neuropathological lesions and dementia become apparent (Carrillo et al., 2013; Dubois et al., 2014). Despite the growing recognition that intervention at the prodromal stage may be needed to treat AD effectively, the biological underpinnings of the AD prodrome have been poorly understood. On the one hand, Rab5-mediated endosomal dysfunction occurs very early in AD (Nixon, 2017) and has been thought to contribute to the preclinical/prodromal phase, although its effects on the neurodegenerative phase of the disease were not considered (Mufson et al., 2016). On the other hand, a soluble form of Aβ peptide at the prodromal stage is most commonly proposed to be the trigger of the neurodegenerative phase of AD by also promoting the dysregulation of tau homeostasis (De Strooper and Karran, 2016; Mufson et al., 2016). However, evidence implicating Aβ as the key prodromal factor initiating the progression

(G) Representative confocal images of PHF-1 and CP13 in layer V cortical neurons from 15-month-old mouse tissue sections. Scale bars, 5 μm.
(H) Quantification of PHF-1 and CP13 neuronal perikaryal intensities within layers II/III and V, relative to WT (mean fluorescence intensities were calculated from n = 17 and n = 12–14 fields at 40×, respectively, from n = 3 mice/genotype).
(I) Representative confocal images of PHF-1 (top) and CP13 (bottom, arrows) in layer II/III cortical neurons of 15-month-old mice. Scale bars, 5 μm.
(J) Quantification of PHF-1 (top) and CP13 (bottom) intensity distributions of layer II/III cortical neurons above threshold, relative to WT (PHF-1 counts: WT n = 143 neurons, PA-Rab5 n = 288 neurons, CP13 counts: WT n = 42 neurons, PA-Rab5 n = 81 neurons).
(K) Double IF staining of PHF-1 (red) and Rab5a (green) shows co-localization in PA-Rab5 layer II/III neurons (K, top panel). Scale bar, 20 μm. Higher-power images show PHF-1 and Rab5 vesicular co-localization in the cell body (arrows). Scale bar, 5 μm. (K, bottom panel) Double IF of CP13 (red) with Rab5a (green) shows partial co-localization. Scale bars, 10 μm. A higher-power image of a double $CP13^+$ and $Rab5^+$ neuron reveals abnormal cell body morphology with less punctate CP13 and Rab5 immunoreactivities (arrows). Scale bar, 5 μm. Images are representative of at least n = 2 sections per n = 3 mice/genotype.
NS, not significant; *p < 0.05; **p < 0.01; ***p < 0.001; ****p < 0.0001; 2-tailed Student's t test. Data are means ± SEMs.

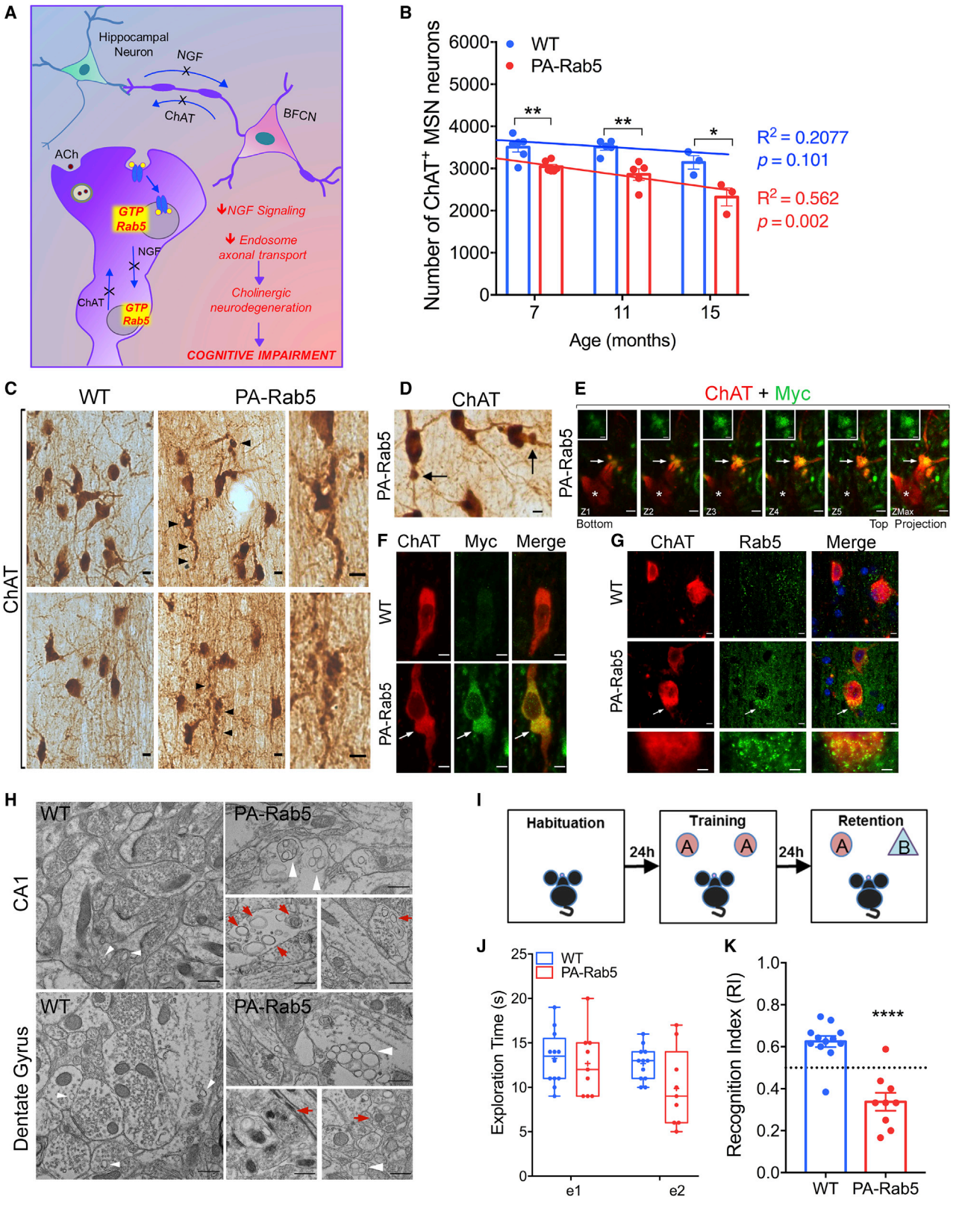

(legend on next page)

of the disease has been limited, despite dominating the conceptualization of therapeutic interventions for AD. Our PA-Rab5 mouse model of pathological Rab5 activation is based on the earliest neuronal pathobiology known in AD, endosomal dysfunction. While APP-βCTF is the main trigger for this endosome dysfunction in AD (Kim et al., 2016; Xu et al., 2016), our approach has revealed diverse contributions of overactivated Rab5 to disease progression, independent of APP-βCTF. Of importance, consequences of this later pathobiology can be evaluated in PA-Rab5 mice unconfounded by the superimposed neurotoxicity of β-amyloidosis and its associated downstream effects (Carrillo et al., 2013; Dubois et al., 2014).

The results of this study underscore the exceptional utility of this approach in revealing diverse prodromal cellular and functional abnormalities, which include AD-related endosomal dysfunction (Cataldo et al., 2000; Kim et al., 2016; Xu et al., 2016), striking synaptic plasticity deficits (Baglietto-Vargas et al., 2018; Bourgeois et al., 2018; Hsieh et al., 2006), and selective tau hyperphosphorylation (Lewis and Dickson, 2016; Muratore et al., 2017) via GSK-3β at AD-related epitopes (Hooper et al., 2008; Israel et al., 2012; Mondragón-Rodríguez et al., 2014)—all of which are consistent with abnormal signaling resulting from overactivated Rab5 and now demonstrated *in vivo* in this report. Intraneuronal Aβ and elevated APP-βCTF, the principal factor initiating Rab5 activation in AD, would normally also be part of this prodromal phase (Gouras et al., 2010; Nixon, 2017). Extracellular Aβ has also been implicated in early neuronal dysfunction occurring in the absence of amyloid plaques. Aβ oligomers and AD brain-derived dimers have been shown to impair synaptic plasticity and neuritic integrity (Brinkmalm et al., 2019; Shankar et al., 2008) and to induce an early and reversible neuronal hyperactivity *in vivo*, possibly by suppressing glutamate reuptake (Stargardt et al., 2015; Zott et al., 2019). How an early increased excitability reconciles with reduced synaptic transmission in AD is still debated. In our model, however, we have activated Rab5 downstream of an APP-related trigger and further shown that endocytic dysfunction did not directly perturb APP processing, thereby bypassing additional pathogenic contributions from altered Aβ or APP-βCTF levels. That said, a notable implication of our study is that the pathological effects exerted by Rab5 overactivation further validate the pathogenic significance of APP-βCTF, the usual trigger for this Rab5 endosomal dysfunction, as supported by mounting evidence (Bourgeois et al., 2018; Israel et al., 2012; Kim et al., 2016; Kwart et al., 2019; Xu et al., 2016).

Equally important as these prodromal effects, our study has uncovered delayed consequences of persistent Rab5 activation that are conventionally associated with the degenerative/clinical stages of AD. Most notably, these include the dystrophy and progressive loss of cholinergic neurons in the basal forebrain, a neuronal population considered to be among the most vulnerable to dysfunction at the earliest stages of AD (Chen and Mobley, 2019; Colacurcio et al., 2018; Nixon, 2017) and additional cognitive deficits characteristic of AD and DS (Granholm et al., 2000; Grothe et al., 2012). Aβ and tau oligomers have been recently proposed to lead to basal forebrain cholinergic neurodegeneration (Chen and Mobley, 2019). However, it is unclear whether these oligomers in fact perturb endosomal homeostasis, and there is no evidence of Aβ or tau activating Rab5. By contrast, our results show that Rab5 overactivation is sufficient to induce an age-dependent loss of cholinergic neurons without an elevation of Aβ levels. As a likely basis for the cholinergic deficits, our characterizations identify neuritic accumulations of endosomes reflecting endosome transport deficits, due to Rab5-mediated impaired endosome retrograde transport (Kim et al., 2016; Xu et al., 2016), and defective endosome-mediated signaling by nerve growth factor (NGF) (Chen and Mobley, 2019; Salehi et al., 2006; Xu et al., 2016) and other neurotrophins (Chen et al., 2018), previously shown in live imaging studies of cultured primary neurons. Further evidence of hippocampal neuritic

Figure 5. Overactivated Rab5 *In Vivo* Induces Cholinergic Neuron Degeneration, Hippocampal Abnormalities, and Memory Impairment

(A) Schematic diagram of the role of Rab5 overactivation in dysregulating retrograde trafficking and signaling of NGF, and anterograde transport of ChAT, leading to BFCN degeneration and cognitive deficits.

(B) Stereological counting of ChAT$^+$ neurons in the MSN shows a significant age-dependent decrease in BFCNs in PA-Rab5, compared to WT (for each age group: 7 months WT and PA-Rab5 n = 6, 11 months WT and PA-Rab5 n = 5, 15 months WT and PA-Rab5 n = 3; linear regression: WT $F_{(1,12)} = 3.147$, p = 0.1014; PA-Rab5 $F_{(1,12)} = 15.39$, p = 0.0020; n = 14 age points).

(C) Representative diaminobenzidine (DAB) images of ChAT$^+$ neurons in the MSN of 7-month-old WT and PA-Rab5 mice. ChAT$^+$ fibers in PA-Rab5 appear swollen (upper panel) and dystrophic (lower panel), compared to WT. Abnormal fiber morphologies are highlighted by the arrowheads and shown enlarged in adjacent panels. Scale bars, 10 μm.

(D) PA-Rab5 ChAT$^+$ BFCNs display remarkable thickening of proximal dendrites (arrows).

(E) A 5-μm-thick z stack of a BFCN double labeled with ChAT (red) and Myc-Rab5 (green) show an abnormal proximal dendrite (arrow) accumulating Myc-Rab5 immunoreactivity (inset). The cell body (*) is visible at the bottom of the stack (z1); the proximal dendrite accumulating myc-Rab5 is protruding toward the top layers.

(F) ChAT-myc-Rab5 double$^+$ BFCNs show abnormal bulging and swelling of the cell body (arrow).

(G) Double labeling with ChAT and Rab5a shows the accumulation of Rab5 immunoreactive puncta in PA-Rab5 cell body (arrow and respective enlarged panels). Scale bars, 5 μm; insets in (E) and enlarged panels in (G), 2.5 μm. All images are representative of n = 2/3 sections per n = 3 mice/genotype.

(H) Representative EM images of dendritic and synaptic profiles in CA1 and DG areas of 7-month-old mice. Compared to WT endosomes (white arrowheads), PA-Rab5 show abnormal accumulation of endosomes within single membrane-delimited structures in dendrites of both CA1 and DG areas (PA-Rab5, white arrowheads). PA-Rab5 mice display mild degenerative profiles, consisting of the presence of autophagic structures in dendrites, synaptic terminals, and neurites (PA-Rab5, red arrows). Scale bars, 0.5 μm.

(I–K) Novel object recognition memory test (ORT) in 6-month-old PA-Rab5 and WT littermates.

(I) The ORT paradigm used.

(J) PA-Rab5 and WT mice showed similar total exploration times of both objects during training (e1) and at 24-h retention (e2).

(K) PA-Rab5 performed significantly less than WT at 24-h retention (WT n = 12, PA-Rab5 n = 9).

*p < 0.05; **p < 0.01; ****p < 0.0001; 2-tailed Student's t test. Data are means ± SEMs.

swellings containing larger accumulations of endosomes and autophagic vesicles further substantiate the early stages of neurodegeneration in vulnerable neuronal populations (Colacurcio et al., 2018). In addition, the Rab5-mediated neurodegenerative phase induced by Rab5 overactivation includes significant losses of hippocampal dendritic spines, a possible underlying basis for aging-related LTP changes and memory decline. In fact, 15-month-old PA-Rab5 showed functional deficits to a greater extent than what we observed (data not shown), but not at 3 months, further supporting the idea that Rab5-mediated effects on synaptic morphology, transmission, and behavior are progressive, rather than developmental. While reports on previous mouse models may have ascribed these pathogenic events to amyloid neurotoxicity, our ability to dissociate Rab5 activation from its APP-related trigger clearly establishes that Rab5 overactivation is sufficient to mediate these events.

Our results establish Rab5 overactivation as a therapeutic target for AD and further suggest that components of the multiple cell signaling pathways regulating Rab5 activation/deactivation (Cavalli et al., 2001), including multiple GEFs, GTPase-activating proteins (GAPs) and guanyl nucleotide dissociation inhibitor (GDI) (Stenmark, 2009), and endocytic genes implicated as AD risk genes (Karch and Goate, 2015; Lambert et al., 2013) represent an additional family of potential therapeutic targets. Furthermore, targeting Rab5 overactivation may prove to be useful in other neurodegenerative conditions involving endosomal-lysosomal trafficking and signaling defects (Kiral et al., 2018). In Parkinson disease (PD), both leucine-rich repeat kinase 2 (LRRK2) and α-synuclein (α-SYN) have been shown to interact with Rab5 (Shi et al., 2017). LRRK2 pathogenic mutations result in the dysregulation of synaptic vesicle endocytosis and trafficking (Shin et al., 2008). Transgenic expression of α-SYN in a mouse model of PD caused Rab5 overactivation, Rab5 positive endosome enlargement, and decreased retrograde transport of neurotrophic signaling leading to neuronal atrophy (Fang et al., 2017). The protein product of *C9ORF72*, linked to amyotrophic lateral sclerosis (ALS)/frontotemporal dementia (FTD) (Renton et al., 2011), and that of *ALS2*/Alsin, linked to ALS 2 (Hadano et al., 2001), exhibit RabGEF activity (Topp et al., 2004; Yang et al., 2001) and have been shown to colocalize with Rab5 on endosomes (Farg et al., 2014; Tang, 2016) or on mitochondria upon stress induction (Hsu et al., 2018), respectively. Finally, in Huntington disease (HD), the Rab5 effector huntingtin (Htt)-associated protein 40 (HAP40) recruits Htt to early endosomes affecting early endosomal motility (Pal et al., 2006), and possibly, impaired retrograde neurotrophin signaling through Rab5 (Liot et al., 2013).

Reducing elevated levels of APP-βCTF to normalize Rab5 overactivation in a model of DS (Ts2 mice) (Jiang et al., 2016) has been shown to rescue endosome dysfunction and cholinergic deficits; however, with this intervention, the specific contribution of Rab5 to the rescue could not be clearly distinguished from Rab5-independent actions of APP. This limitation has been addressed, however, in our recent studies (Alam et al., 2017; Jiang et al., 2019b) showing that blocking Rab5 with a selective p38 inhibitor possibly by overactivation by inhibiting GDI (Cavalli et al., 2001; Alam, 2015) rescued endosomal enlargement and cholinergic neurodegeneration in a mouse model of DS (Ts2) as effectively as reversing elevated APP-βCTF levels (Jiang et al., 2016). Notably, recent results from a phase IIb clinical trial on p38α inhibitor in early-stage AD (https://clinicaltrials.gov/ct2/show/NCT03402659) demonstrated the effectiveness of a p38α inhibitor relative to placebo in significantly reducing cerebrospinal fluid (CSF) levels of p-tau and tau, major markers of neurodegeneration and axonal damage. Although it has been a theoretical concern that targeting endosome dysfunction could abrogate the essential functions of endocytosis, our recent observations demonstrate that AD-related Rab5 hyperactivation is a pathological process superimposed upon physiological Rab5 activation (Jiang et al., 2016; Kim et al., 2016; data not shown) and, therefore, can be corrected without depressing physiological Rab5 activation or its associated endocytic functions (Alam et al., 2017; Jiang et al., 2019b; Kim et al., 2016).

In conclusion, our study shows that Rab5 overactivation is sufficient to induce endosomal dysfunction. Our results implicate Rab5 as a major driver of both very early and later degenerative and cognitive deficits during AD development, suggesting a continuous Rab5-dependent prodromal to degenerative cascade paralleling, and independent of, the β-amyloid cascade. Lastly, our results suggest the regulation of Rab5 overactivation as a promising therapeutic target for AD and, possibly, for other neurodegenerative conditions involving endosomal trafficking defects such as PD, ALS/FTD, and HD. The PA-Rab5 mouse represents an example of a generation of AD models that enable the validation of therapeutic targets within this additional pathogenic pathway paralleling the β-amyloid cascade, but unconfounded by superimposed Aβ/β-amyloid-associated neurotoxicity.

STAR★METHODS

Detailed methods are provided in the online version of this paper and include the following:

- KEY RESOURCES TABLE
- RESOURCE AVAILABILITY
  - Lead Contact
  - Materials Availability
  - Data and Code Availability
- EXPERIMENTAL MODEL AND SUBJECT DETAILS
- METHOD DETAILS
  - Immunofluorescence and diaminobenzidine (DAB) staining
  - Morphometric analyses
  - Electron microscopy and immunogold EM
  - Electrophysiology
  - Novel Object recognition
  - Golgi staining for spine density and morphology
  - Stereological counting of MSN-ChAT cells
  - Surface biotinylation of acute hippocampal slices and sample homogenization for biochemical analysis
  - Synaptosome isolation
  - Rab5-GTP pull-down assays from hippocampal homogenates and synaptosomes
  - Hippocampal endosome-enriched cytosol (EEcyt) preparation for Rab5-GTP and RabGEF-1 IP

- Endosome isolation
- Tissue preparation for Western Blot and ELISA and primary antibodies
- Sandwich ELISA

● QUANTIFICATION AND STATISTICAL ANALYSIS

SUPPLEMENTAL INFORMATION

Supplemental Information can be found online at https://doi.org/10.1016/j.celrep.2020.108420.

ACKNOWLEDGMENTS

We wish to thank Dr. Masuo Ohno (Nathan S. Kline Institute) for his generous gift of 5XFAD mice and Dr. Efrat Levy (Nathan S. Kline Institute), Dr. John Alam (EIP Pharma), and Dr. Lauren Whyte (Nathan S. Kline Institute) for critical reading of the manuscript. This work was supported by NIH P01AG017617 and R01AG062376 to R.A.N.

AUTHOR CONTRIBUTIONS

Conceptualization, R.A.N.; Methodology, A.P., S.K., and R.A.N.; Validation, A.P., Y.J., J.-H.L., and M.J.B.; Formal Analysis, A.P., S.S., C.B., Y.J., S.D., M.J.B., J.F.S., and B.S.B.; Investigation, A.P., S.K., S.S., C.B., C.N.G., P.H.S., Y.J., J.-H.L., J.P., M.J.B., J.F.S., and B.S.B.; Resources, A.P., S.S., C.B., C.N.G., Y.J., J.-H.L., M.P., C.H., M.J.B., J.F.S., and B.S.B.; Writing – Original Draft, A.P. and R.A.N.; Writing – Review & Editing, A.P., P.H.S., Y.J., J.-H.L., M.J.B., and R.A.N.; Supervision, R.A.N.; Funding Acquisition, R.A.N.

DECLARATION OF INTERESTS

The authors declare no competing interests.

Received: December 17, 2019
Revised: June 5, 2020
Accepted: November 2, 2020
Published: November 24, 2020

REFERENCES

Alam, J.J. (2015). Selective Brain-Targeted Antagonism of p38 MAPKα Reduces Hippocampal IL-1β Levels and Improves Morris Water Maze Performance in Aged Rats. J. Alzheimers Dis. *48*, 219–227.

Alam, J., Jiang, Y., and Nixon, R. (2017). Antagonism of P38 MAPK alpha (P38α) reverses APP-induced endosomal abnormalities and improves lysosomal function in Down syndrome fibroblasts. Alzheimers Dement. *13*, P1496–P1497.

Androuin, A., Potier, B., Nägerl, U.V., Cattaert, D., Danglot, L., Thierry, M., Youssef, I., Triller, A., Duyckaerts, C., El Hachimi, K.H., et al. (2018). Evidence for altered dendritic spine compartmentalization in Alzheimer's disease and functional effects in a mouse model. Acta Neuropathol. *135*, 839–854.

Baglietto-Vargas, D., Prieto, G.A., Limon, A., Forner, S., Rodriguez-Ortiz, C.J., Ikemura, K., Ager, R.R., Medeiros, R., Trujillo-Estrada, L., Martini, A.C., et al. (2018). Impaired AMPA signaling and cytoskeletal alterations induce early synaptic dysfunction in a mouse model of Alzheimer's disease. Aging Cell *17*, e12791.

Ballinger, E.C., Ananth, M., Talmage, D.A., and Role, L.W. (2016). Basal Forebrain Cholinergic Circuits and Signaling in Cognition and Cognitive Decline. Neuron *91*, 1199–1218.

Barlow, J.Z., and Huntley, G.W. (2000). Developmentally regulated expression of Thy-1 in structures of the mouse sensory-motor system. J. Comp. Neurol. *421*, 215–233.

Belichenko, P.V., Masliah, E., Kleschevnikov, A.M., Villar, A.J., Epstein, C.J., Salehi, A., and Mobley, W.C. (2004). Synaptic structural abnormalities in the Ts65Dn mouse model of Down Syndrome. J. Comp. Neurol. *480*, 281–298.

Bourgeois, A., Lauritzen, I., Lorivel, T., Bauer, C., Checler, F., and Pardossi-Piquard, R. (2018). Intraneuronal accumulation of C99 contributes to synaptic alterations, apathy-like behavior, and spatial learning deficits in 3×TgAD and 2×TgAD mice. Neurobiol. Aging *71*, 21–31.

Brinkmalm, G., Hong, W., Wang, Z., Liu, W., O'Malley, T.T., Sun, X., Frosch, M.P., Selkoe, D.J., Portelius, E., Zetterberg, H., et al. (2019). Identification of neurotoxic cross-linked amyloid-β dimers in the Alzheimer's brain. Brain *142*, 1441–1457.

Brown, T.C., Tran, I.C., Backos, D.S., and Esteban, J.A. (2005). NMDA receptor-dependent activation of the small GTPase Rab5 drives the removal of synaptic AMPA receptors during hippocampal LTD. Neuron *45*, 81–94.

Calafate, S., Flavin, W., Verstreken, P., and Moechars, D. (2016). Loss of Bin1 Promotes the Propagation of Tau Pathology. Cell Rep. *17*, 931–940.

Carrillo, M.C., Dean, R.A., Nicolas, F., Miller, D.S., Berman, R., Khachaturian, Z., Bain, L.J., Schindler, R., and Knopman, D.; Alzheimer's Association Research Roundtable (2013). Revisiting the framework of the National Institute on Aging-Alzheimer's Association diagnostic criteria. Alzheimers Dement. *9*, 594–601.

Cataldo, A.M., Barnett, J.L., Pieroni, C., and Nixon, R.A. (1997). Increased neuronal endocytosis and protease delivery to early endosomes in sporadic Alzheimer's disease: neuropathologic evidence for a mechanism of increased beta-amyloidogenesis. J. Neurosci. *17*, 6142–6151.

Cataldo, A.M., Peterhoff, C.M., Troncoso, J.C., Gomez-Isla, T., Hyman, B.T., and Nixon, R.A. (2000). Endocytic pathway abnormalities precede amyloid beta deposition in sporadic Alzheimer's disease and Down syndrome: differential effects of APOE genotype and presenilin mutations. Am. J. Pathol. *157*, 277–286.

Cataldo, A.M., Petanceska, S., Terio, N.B., Peterhoff, C.M., Durham, R., Mercken, M., Mehta, P.D., Buxbaum, J., Haroutunian, V., and Nixon, R.A. (2004). Abeta localization in abnormal endosomes: association with earliest Abeta elevations in AD and Down syndrome. Neurobiol. Aging *25*, 1263–1272.

Cataldo, A.M., Mathews, P.M., Boiteau, A.B., Hassinger, L.C., Peterhoff, C.M., Jiang, Y., Mullaney, K., Neve, R.L., Gruenberg, J., and Nixon, R.A. (2008). Down syndrome fibroblast model of Alzheimer-related endosome pathology: accelerated endocytosis promotes late endocytic defects. Am. J. Pathol. *173*, 370–384.

Cavalli, V., Vilbois, F., Corti, M., Marcote, M.J., Tamura, K., Karin, M., Arkinstall, S., and Gruenberg, J. (2001). The stress-induced MAP kinase p38 regulates endocytic trafficking via the GDI:Rab5 complex. Mol. Cell *7*, 421–432.

Chen, X.Q., and Mobley, W.C. (2019). Exploring the Pathogenesis of Alzheimer Disease in Basal Forebrain Cholinergic Neurons: Converging Insights From Alternative Hypotheses. Front. Neurosci. *13*, 446.

Chen, X.Q., Sawa, M., and Mobley, W.C. (2018). Dysregulation of neurotrophin signaling in the pathogenesis of Alzheimer disease and of Alzheimer disease in Down syndrome. Free Radic. Biol. Med. *114*, 52–61.

Chow, H.M., Guo, D., Zhou, J.C., Zhang, G.Y., Li, H.F., Herrup, K., and Zhang, J. (2014). CDK5 activator protein p25 preferentially binds and activates GSK3β. Proc. Natl. Acad. Sci. USA *111*, E4887–E4895.

Christoforidis, S., and Zerial, M. (2000). Purification and identification of novel Rab effectors using affinity chromatography. Methods *20*, 403–410.

Colacurcio, D.J., Pensalfini, A., Jiang, Y., and Nixon, R.A. (2018). Dysfunction of autophagy and endosomal-lysosomal pathways: roles in pathogenesis of Down syndrome and Alzheimer's disease. Free Radic. Biol. Med. *114*, 40–51.

Cormont, M., Metón, I., Mari, M., Monzo, P., Keslair, F., Gaskin, C., McGraw, T.E., and Le Marchand-Brustel, Y. (2003). CD2AP/CMS regulates endosome morphology and traffic to the degradative pathway through its interaction with Rab4 and c-Cbl. Traffic *4*, 97–112.

David, C., McPherson, P.S., Mundigl, O., and de Camilli, P. (1996). A role of amphiphysin in synaptic vesicle endocytosis suggested by its binding to dynamin in nerve terminals. Proc. Natl. Acad. Sci. USA *93*, 331–335.

De Strooper, B., and Karran, E. (2016). The Cellular Phase of Alzheimer's Disease. Cell *164*, 603–615.

Dou, Z., Pan, J.A., Dbouk, H.A., Ballou, L.M., DeLeon, J.L., Fan, Y., Chen, J.S., Liang, Z., Li, G., Backer, J.M., et al. (2013). Class IA PI3K p110β subunit promotes autophagy through Rab5 small GTPase in response to growth factor limitation. Mol. Cell *50*, 29–42.

Dubois, B., Feldman, H.H., Jacova, C., Hampel, H., Molinuevo, J.L., Blennow, K., DeKosky, S.T., Gauthier, S., Selkoe, D., Bateman, R., et al. (2014). Advancing research diagnostic criteria for Alzheimer's disease: the IWG-2 criteria. Lancet Neurol. *13*, 614–629.

Eimer, W.A., and Vassar, R. (2013). Neuron loss in the 5XFAD mouse model of Alzheimer's disease correlates with intraneuronal Aβ42 accumulation and Caspase-3 activation. Mol. Neurodegener. *8*, 2.

Fang, F., Yang, W., Florio, J.B., Rockenstein, E., Spencer, B., Orain, X.M., Dong, S.X., Li, H., Chen, X., Sung, K., et al. (2017). Synuclein impairs trafficking and signaling of BDNF in a mouse model of Parkinson's disease. Sci. Rep. *7*, 3868.

Farg, M.A., Sundaramoorthy, V., Sultana, J.M., Yang, S., Atkinson, R.A., Levina, V., Halloran, M.A., Gleeson, P.A., Blair, I.P., Soo, K.Y., et al. (2014). C9ORF72, implicated in amytrophic lateral sclerosis and frontotemporal dementia, regulates endosomal trafficking. Hum. Mol. Genet. *23*, 3579–3595.

Fjorback, A.W., and Andersen, O.M. (2012). SorLA is a molecular link for retromer-dependent sorting of the Amyloid precursor protein. Commun. Integr. Biol. *5*, 616–619.

Ginsberg, S.D., Alldred, M.J., Counts, S.E., Cataldo, A.M., Neve, R.L., Jiang, Y., Wuu, J., Chao, M.V., Mufson, E.J., Nixon, R.A., and Che, S. (2010a). Microarray analysis of hippocampal CA1 neurons implicates early endosomal dysfunction during Alzheimer's disease progression. Biol. Psychiatry *68*, 885–893.

Ginsberg, S.D., Mufson, E.J., Counts, S.E., Wuu, J., Alldred, M.J., Nixon, R.A., and Che, S. (2010b). Regional selectivity of rab5 and rab7 protein upregulation in mild cognitive impairment and Alzheimer's disease. J. Alzheimers Dis. *22*, 631–639.

Ginsberg, S.D., Mufson, E.J., Alldred, M.J., Counts, S.E., Wuu, J., Nixon, R.A., and Che, S. (2011). Upregulation of select rab GTPases in cholinergic basal forebrain neurons in mild cognitive impairment and Alzheimer's disease. J. Chem. Neuroanat. *42*, 102–110.

Gorvel, J.P., Chavrier, P., Zerial, M., and Gruenberg, J. (1991). rab5 controls early endosome fusion in vitro. Cell *64*, 915–925.

Goto-Silva, L., McShane, M.P., Salinas, S., Kalaidzidis, Y., Schiavo, G., and Zerial, M. (2019). Retrograde transport of Akt by a neuronal Rab5-APPL1 endosome. Sci. Rep. *9*, 2433.

Gouras, G.K., Tampellini, D., Takahashi, R.H., and Capetillo-Zarate, E. (2010). Intraneuronal beta-amyloid accumulation and synapse pathology in Alzheimer's disease. Acta Neuropathol. *119*, 523–541.

Granholm, A.C., Sanders, L.A., and Crnic, L.S. (2000). Loss of cholinergic phenotype in basal forebrain coincides with cognitive decline in a mouse model of Down's syndrome. Exp. Neurol. *161*, 647–663.

Grothe, M., Heinsen, H., and Teipel, S.J. (2012). Atrophy of the cholinergic basal forebrain over the adult age range and in early stages of Alzheimer's disease. Biol. Psychiatry *71*, 805–813.

Gruenberg, J., Griffiths, G., and Howell, K.E. (1989). Characterization of the early endosome and putative endocytic carrier vesicles in vivo and with an assay of vesicle fusion in vitro. J. Cell Biol. *108*, 1301–1316.

Haam, J., and Yakel, J.L. (2017). Cholinergic modulation of the hippocampal region and memory function. J. Neurochem. *142* (*Suppl 2*), 111–121.

Haas, M.A., Bell, D., Slender, A., Lana-Elola, E., Watson-Scales, S., Fisher, E.M., Tybulewicz, V.L., and Guillemot, F. (2013). Alterations to dendritic spine morphology, but not dendrite patterning, of cortical projection neurons in Tc1 and Ts1Rhr mouse models of Down syndrome. PLOS ONE *8*, e78561.

Hadano, S., Hand, C.K., Osuga, H., Yanagisawa, Y., Otomo, A., Devon, R.S., Miyamoto, N., Showguchi-Miyata, J., Okada, Y., Singaraja, R., et al. (2001). A gene encoding a putative GTPase regulator is mutated in familial amyotrophic lateral sclerosis 2. Nat. Genet. *29*, 166–173.

Harel, A., Wu, F., Mattson, M.P., Morris, C.M., and Yao, P.J. (2008). Evidence for CALM in directing VAMP2 trafficking. Traffic *9*, 417–429.

Hausser, A., and Schlett, K. (2019). Coordination of AMPA receptor trafficking by Rab GTPases. Small GTPases *10*, 419–432.

Hooper, C., Killick, R., and Lovestone, S. (2008). The GSK3 hypothesis of Alzheimer's disease. J. Neurochem. *104*, 1433–1439.

Horiuchi, H., Lippé, R., McBride, H.M., Rubino, M., Woodman, P., Stenmark, H., Rybin, V., Wilm, M., Ashman, K., Mann, M., and Zerial, M. (1997). A novel Rab5 GDP/GTP exchange factor complexed to Rabaptin-5 links nucleotide exchange to effector recruitment and function. Cell *90*, 1149–1159.

Hsieh, H., Boehm, J., Sato, C., Iwatsubo, T., Tomita, T., Sisodia, S., and Malinow, R. (2006). AMPAR removal underlies Abeta-induced synaptic depression and dendritic spine loss. Neuron *52*, 831–843.

Hsu, F., Spannl, S., Ferguson, C., Hyman, A.A., Parton, R.G., and Zerial, M. (2018). Rab5 and Alsin regulate stress-activated cytoprotective signaling on mitochondria. eLife *7*, e32282.

Hung, H., and Livesey, F.J. (2018). Altered γ-Secretase Processing of APP Disrupts Lysosome and TitAutophagosome Function in Monogenic Alzheimer's Disease. Cell Rep. *25*, 3647–3660.e2.

Ishikawa, Y., Okada, M., Honda, A., Ito, Y., Tamada, A., Endo, N., and Igarashi, M. (2019). Phosphorylation sites of microtubule-associated protein 1B (MAP 1B) are involved in axon growth and regeneration. Mol. Brain *12*, 93.

Israel, M.A., Yuan, S.H., Bardy, C., Reyna, S.M., Mu, Y., Herrera, C., Hefferan, M.P., Van Gorp, S., Nazor, K.L., Boscolo, F.S., et al. (2012). Probing sporadic and familial Alzheimer's disease using induced pluripotent stem cells. Nature *482*, 216–220.

Iulita, M.F., and Cuello, A.C. (2016). The NGF Metabolic Pathway in the CNS and its Dysregulation in Down Syndrome and Alzheimer's Disease. Curr. Alzheimer Res. *13*, 53–67.

Jiang, Y., Mullaney, K.A., Peterhoff, C.M., Che, S., Schmidt, S.D., Boyer-Boiteau, A., Ginsberg, S.D., Cataldo, A.M., Mathews, P.M., and Nixon, R.A. (2010). Alzheimer's-related endosome dysfunction in Down syndrome is Abeta-independent but requires APP and is reversed by BACE-1 inhibition. Proc. Natl. Acad. Sci. USA *107*, 1630–1635.

Jiang, Y., Rigoglioso, A., Peterhoff, C.M., Pawlik, M., Sato, Y., Bleiwas, C., Stavrides, P., Smiley, J.F., Ginsberg, S.D., Mathews, P.M., et al. (2016). Partial BACE1 reduction in a Down syndrome mouse model blocks Alzheimer-related endosomal anomalies and cholinergic neurodegeneration: role of APP-CTF. Neurobiol. Aging *39*, 90–98.

Jiang, Y., Sato, Y., Im, E., Berg, M., Bordi, M., Darji, S., Kumar, A., Mohan, P.S., Bandyopadhyay, U., Diaz, A., et al. (2019a). Lysosomal Dysfunction in Down Syndrome Is APP-Dependent and Mediated by APP-βCTF (C99). J. Neurosci. *39*, 5255–5268.

Jiang, Y., Stavrides, P., Darji, S., Yang, D.-S., Bleiwas, C., Smiley, J., Germann, U., Alam, J., and Nixon, R. (2019b). Effects of P38α MAP kinase inhibition on the neurodegenerative phenotype of the TS2 Down syndrome mouse model. Alzheimers Dement. *15*, 1597.

Joshi, V., Subbanna, S., Shivakumar, M., and Basavarajappa, B.S. (2019). CB1R regulates CDK5 signaling and epigenetically controls Rac1 expression contributing to neurobehavioral abnormalities in mice postnatally exposed to ethanol. Neuropsychopharmacology *44*, 514–525.

Kajiho, H., Saito, K., Tsujita, K., Kontani, K., Araki, Y., Kurosu, H., and Katada, T. (2003). RIN3: a novel Rab5 GEF interacting with amphiphysin II involved in the early endocytic pathway. J. Cell Sci. *116*, 4159–4168.

Karch, C.M., and Goate, A.M. (2015). Alzheimer's disease risk genes and mechanisms of disease pathogenesis. Biol. Psychiatry *77*, 43–51.

Kim, S., Sato, Y., Mohan, P.S., Peterhoff, C., Pensalfini, A., Rigoglioso, A., Jiang, Y., and Nixon, R.A. (2016). Evidence that the rab5 effector APPL1 mediates APP-βCTF-induced dysfunction of endosomes in Down syndrome and Alzheimer's disease. Mol. Psychiatry *21*, 707–716.

Kiral, F.R., Kohrs, F.E., Jin, E.J., and Hiesinger, P.R. (2018). Rab GTPases and Membrane Trafficking in Neurodegeneration. Curr. Biol. *28*, R471–R486.

Kwart, D., Gregg, A., Scheckel, C., Murphy, E., Paquet, D., Duffield, M., Fak, J., Olsen, O., Darnell, R., and Tessier-Lavigne, M. (2019). A Large Panel of Isogenic APP and PSEN1 Mutant Human iPSC Neurons Reveals Shared Endosomal Abnormalities Mediated by APP beta-CTFs, Not Abeta. Neuron *104*, 256–270.e5.

Lambert, J.C., Ibrahim-Verbaas, C.A., Harold, D., Naj, A.C., Sims, R., Bellenguez, C., DeStafano, A.L., Bis, J.C., Beecham, G.W., Grenier-Boley, B., et al.; European Alzheimer's Disease Initiative (EADI); Genetic and Environmental Risk in Alzheimer's Disease; Alzheimer's Disease Genetic Consortium; Cohorts for Heart and Aging Research in Genomic Epidemiology (2013). Meta-analysis of 74,046 individuals identifies 11 new susceptibility loci for Alzheimer's disease. Nat. Genet. *45*, 1452–1458.

Lee, H.K., Barbarosie, M., Kameyama, K., Bear, M.F., and Huganir, R.L. (2000). Regulation of distinct AMPA receptor phosphorylation sites during bidirectional synaptic plasticity. Nature *405*, 955–959.

Lee, J.H., Rao, M.V., Yang, D.S., Stavrides, P., Im, E., Pensalfini, A., Huo, C., Sarkar, P., Yoshimori, T., and Nixon, R.A. (2019). Transgenic expression of a ratiometric autophagy probe specifically in neurons enables the interrogation of brain autophagy in vivo. Autophagy *15*, 543–557.

Lewis, J., and Dickson, D.W. (2016). Propagation of tau pathology: hypotheses, discoveries, and yet unresolved questions from experimental and human brain studies. Acta Neuropathol. *131*, 27–48.

Lin, Y.T., Seo, J., Gao, F., Feldman, H.M., Wen, H.L., Penney, J., Cam, H.P., Gjoneska, E., Raja, W.K., Cheng, J., et al. (2018). APOE4 Causes Widespread Molecular and Cellular Alterations Associated with Alzheimer's Disease Phenotypes in Human iPSC-Derived Brain Cell Types. Neuron *98*, 1141–1154.e7.

Liot, G., Zala, D., Pla, P., Mottet, G., Piel, M., and Saudou, F. (2013). Mutant Huntingtin alters retrograde transport of TrkB receptors in striatal dendrites. J. Neurosci. *33*, 6298–6309.

Lippé, R., Miaczynska, M., Rybin, V., Runge, A., and Zerial, M. (2001). Functional synergy between Rab5 effector Rabaptin-5 and exchange factor Rabex-5 when physically associated in a complex. Mol. Biol. Cell *12*, 2219–2228.

Liu, J., Lamb, D., Chou, M.M., Liu, Y.J., and Li, G. (2007). Nerve growth factor-mediated neurite outgrowth via regulation of Rab5. Mol. Biol. Cell *18*, 1375–1384.

Liu, C.C., Liu, C.C., Kanekiyo, T., Xu, H., and Bu, G. (2013). Apolipoprotein E and Alzheimer disease: risk, mechanisms and therapy. Nat. Rev. Neurol. *9*, 106–118.

Louneva, N., Cohen, J.W., Han, L.Y., Talbot, K., Wilson, R.S., Bennett, D.A., Trojanowski, J.Q., and Arnold, S.E. (2008). Caspase-3 is enriched in postsynaptic densities and increased in Alzheimer's disease. Am. J. Pathol. *173*, 1488–1495.

Mani, M., Lee, U.H., Yoon, N.A., Kim, H.J., Ko, M.S., Seol, W., Joe, Y., Chung, H.T., Lee, B.J., Moon, C.H., et al. (2016). Developmentally regulated GTP-binding protein 2 coordinates Rab5 activity and transferrin recycling. Mol. Biol. Cell *27*, 334–348.

Martin, S.A., Souder, D.C., Miller, K.N., Clark, J.P., Sagar, A.K., Eliceiri, K.W., Puglielli, L., Beasley, T.M., and Anderson, R.M. (2018). GSK3β Regulates Brain Energy Metabolism. Cell Rep. *23*, 1922–1931.e4.

Mathews, P.M., Guerra, C.B., Jiang, Y., Grbovic, O.M., Kao, B.H., Schmidt, S.D., Dinakar, R., Mercken, M., Hille-Rehfeld, A., Rohrer, J., et al. (2002). Alzheimer's disease-related overexpression of the cation-dependent mannose 6-phosphate receptor increases Abeta secretion: role for altered lysosomal hydrolase distribution in beta-amyloidogenesis. J. Biol. Chem. *277*, 5299–5307.

Miranda, A.M., Lasiecka, Z.M., Xu, Y., Neufeld, J., Shahriar, S., Simoes, S., Chan, R.B., Oliveira, T.G., Small, S.A., and Di Paolo, G. (2018). Neuronal lysosomal dysfunction releases exosomes harboring APP C-terminal fragments and unique lipid signatures. Nat. Commun. *9*, 291.

Mondragón-Rodríguez, S., Perry, G., Luna-Muñoz, J., Acevedo-Aquino, M.C., and Williams, S. (2014). Phosphorylation of tau protein at sites Ser(396-404) is one of the earliest events in Alzheimer's disease and Down syndrome. Neuropathol. Appl. Neurobiol. *40*, 121–135.

Mufson, E.J., Ikonomovic, M.D., Counts, S.E., Perez, S.E., Malek-Ahmadi, M., Scheff, S.W., and Ginsberg, S.D. (2016). Molecular and cellular pathophysiology of preclinical Alzheimer's disease. Behav. Brain Res. *311*, 54–69.

Muratore, C.R., Zhou, C., Liao, M., Fernandez, M.A., Taylor, W.M., Lagomarsino, V.N., Pearse, R.V., 2nd, Rice, H.C., Negri, J.M., He, A., et al. (2017). Cell-type Dependent Alzheimer's Disease Phenotypes: Probing the Biology of Selective Neuronal Vulnerability. Stem Cell Reports *9*, 1868–1884.

Muth, K., Schönmeyer, R., Matura, S., Haenschel, C., Schröder, J., and Pantel, J. (2010). Mild cognitive impairment in the elderly is associated with volume loss of the cholinergic basal forebrain region. Biol. Psychiatry *67*, 588–591.

Nixon, R.A. (2017). Amyloid precursor protein and endosomal-lysosomal dysfunction in Alzheimer's disease: inseparable partners in a multifactorial disease. FASEB J. *31*, 2729–2743.

Nyakas, C., Granic, I., Halmy, L.G., Banerjee, P., and Luiten, P.G. (2011). The basal forebrain cholinergic system in aging and dementia. Rescuing cholinergic neurons from neurotoxic amyloid-β42 with memantine. Behav. Brain Res. *221*, 594–603.

Oakley, H., Cole, S.L., Logan, S., Maus, E., Shao, P., Craft, J., Guillozet-Bongaarts, A., Ohno, M., Disterhoft, J., Van Eldik, L., et al. (2006). Intraneuronal beta-amyloid aggregates, neurodegeneration, and neuron loss in transgenic mice with five familial Alzheimer's disease mutations: potential factors in amyloid plaque formation. J. Neurosci. *26*, 10129–10140.

Pal, A., Severin, F., Lommer, B., Shevchenko, A., and Zerial, M. (2006). Huntingtin-HAP40 complex is a novel Rab5 effector that regulates early endosome motility and is up-regulated in Huntington's disease. J. Cell Biol. *172*, 605–618.

Pera, M., Alcolea, D., Sánchez-Valle, R., Guardia-Laguarta, C., Colom-Cadena, M., Badiola, N., Suárez-Calvet, M., Lladó, A., Barrera-Ocampo, A.A., Sepulveda-Falla, D., et al. (2013). Distinct patterns of APP processing in the CNS in autosomal-dominant and sporadic Alzheimer disease. Acta Neuropathol. *125*, 201–213.

Phillips, G.R., Huang, J.K., Wang, Y., Tanaka, H., Shapiro, L., Zhang, W., Shan, W.S., Arndt, K., Frank, M., Gordon, R.E., et al. (2001). The presynaptic particle web: ultrastructure, composition, dissolution, and reconstitution. Neuron *32*, 63–77.

Rao, M.V., Mohan, P.S., Peterhoff, C.M., Yang, D.S., Schmidt, S.D., Stavrides, P.H., Campbell, J., Chen, Y., Jiang, Y., Paskevich, P.A., et al. (2008). Marked calpastatin (CAST) depletion in Alzheimer's disease accelerates cytoskeleton disruption and neurodegeneration: neuroprotection by CAST overexpression. J. Neurosci. *28*, 12241–12254.

Renton, A.E., Majounie, E., Waite, A., Simón-Sánchez, J., Rollinson, S., Gibbs, J.R., Schymick, J.C., Laaksovirta, H., van Swieten, J.C., Myllykangas, L., et al.; ITALSGEN Consortium (2011). A hexanucleotide repeat expansion in C9ORF72 is the cause of chromosome 9p21-linked ALS-FTD. Neuron *72*, 257–268.

Salehi, A., Delcroix, J.D., Belichenko, P.V., Zhan, K., Wu, C., Valletta, J.S., Takimoto-Kimura, R., Kleschevnikov, A.M., Sambamurti, K., Chung, P.P., et al. (2006). Increased App expression in a mouse model of Down's syndrome disrupts NGF transport and causes cholinergic neuron degeneration. Neuron *51*, 29–42.

Sathiya Priya, C., Vidhya, R., Kalpana, K., and Anuradha, C.V. (2019). Indirubin-3′-monoxime prevents aberrant activation of GSK-3β/NF-κB and alleviates high fat-high fructose induced Aβ-aggregation, gliosis and apoptosis in mice brain. Int. Immunopharmacol. *70*, 396–407.

Schindelin, J., Arganda-Carreras, I., Frise, E., Kaynig, V., Longair, M., Pietzsch, T., Preibisch, S., Rueden, C., Saalfeld, S., Schmid, B., et al. (2012). Fiji: an open-source platform for biological-image analysis. Nat. Methods *9*, 676–682.

Schmidt, S.D., Jiang, Y., Nixon, R.A., and Mathews, P.M. (2005). Tissue processing prior to protein analysis and amyloid-beta quantitation. Methods Mol. Biol. *299*, 267–278.

Schmöle, A.C., Brennführer, A., Karapetyan, G., Jaster, R., Pews-Davtyan, A., Hübner, R., Ortinau, S., Beller, M., Rolfs, A., and Frech, M.J. (2010). Novel indolylmaleimide acts as GSK-3beta inhibitor in human neural progenitor cells. Bioorg. Med. Chem. *18*, 6785–6795.

Shankar, G.M., Li, S., Mehta, T.H., Garcia-Munoz, A., Shepardson, N.E., Smith, I., Brett, F.M., Farrell, M.A., Rowan, M.J., Lemere, C.A., et al. (2008). Amyloid-beta protein dimers isolated directly from Alzheimer's brains impair synaptic plasticity and memory. Nat. Med. *14*, 837–842.

Shi, M.M., Shi, C.H., and Xu, Y.M. (2017). Rab GTPases: The Key Players in the Molecular Pathway of Parkinson's Disease. Front. Cell. Neurosci. *11*, 81.

Shi, M., Chen, B., Mahajan, D., Boh, B.K., Zhou, Y., Dutta, B., Tie, H.C., Sze, S.K., Wu, G., and Lu, L. (2018). Amino acids stimulate the endosome-to-Golgi trafficking through Ragulator and small GTPase Arl5. Nat. Commun. *9*, 4987.

Shin, N., Jeong, H., Kwon, J., Heo, H.Y., Kwon, J.J., Yun, H.J., Kim, C.H., Han, B.S., Tong, Y., Shen, J., et al. (2008). LRRK2 regulates synaptic vesicle endocytosis. Exp. Cell Res. *314*, 2055–2065.

Stargardt, A., Swaab, D.F., and Bossers, K. (2015). Storm before the quiet: neuronal hyperactivity and Aβ in the presymptomatic stages of Alzheimer's disease. Neurobiol. Aging *36*, 1–11.

Stenmark, H. (2009). Rab GTPases as coordinators of vesicle traffic. Nat. Rev. Mol. Cell Biol. *10*, 513–525.

Stenmark, H., Vitale, G., Ullrich, O., and Zerial, M. (1995). Rabaptin-5 is a direct effector of the small GTPase Rab5 in endocytic membrane fusion. Cell *83*, 423–432.

Subbanna, S., Shivakumar, M., Psychoyos, D., Xie, S., and Basavarajappa, B.S. (2013). Anandamide-CB1 receptor signaling contributes to postnatal ethanol-induced neonatal neurodegeneration, adult synaptic, and memory deficits. J. Neurosci. *33*, 6350–6366.

Tackenberg, C., Ghori, A., and Brandt, R. (2009). Thin, stubby or mushroom: spine pathology in Alzheimer's disease. Curr. Alzheimer Res. *6*, 261–268.

Tang, B.L. (2016). C9orf72's Interaction with Rab GTPases-Modulation of Membrane Traffic and Autophagy. Front. Cell. Neurosci. *10*, 228.

Tenreiro, S., Eckermann, K., and Outeiro, T.F. (2014). Protein phosphorylation in neurodegeneration: friend or foe? Front. Mol. Neurosci. *7*, 42.

Thomas-Crusells, J., Vieira, A., Saarma, M., and Rivera, C. (2003). A novel method for monitoring surface membrane trafficking on hippocampal acute slice preparation. J. Neurosci. Methods *125*, 159–166.

Topp, J.D., Gray, N.W., Gerard, R.D., and Horazdovsky, B.F. (2004). Alsin is a Rab5 and Rac1 guanine nucleotide exchange factor. J. Biol. Chem. *279*, 24612–24623.

Xu, W., Weissmiller, A.M., White, J.A., 2nd, Fang, F., Wang, X., Wu, Y., Pearn, M.L., Zhao, X., Sawa, M., Chen, S., et al. (2016). Amyloid precursor protein-mediated endocytic pathway disruption induces axonal dysfunction and neurodegeneration. J. Clin. Invest. *126*, 1815–1833.

Xu, W., Fang, F., Ding, J., and Wu, C. (2018). Dysregulation of Rab5-mediated endocytic pathways in Alzheimer's disease. Traffic *19*, 253–262.

Yang, Y., Hentati, A., Deng, H.X., Dabbagh, O., Sasaki, T., Hirano, M., Hung, W.Y., Ouahchi, K., Yan, J., Azim, A.C., et al. (2001). The gene encoding alsin, a protein with three guanine-nucleotide exchange factor domains, is mutated in a form of recessive amyotrophic lateral sclerosis. Nat. Genet. *29*, 160–165.

Yang, D.S., Lee, J.H., and Nixon, R.A. (2009). Monitoring autophagy in Alzheimer's disease and related neurodegenerative diseases. Methods Enzymol. *453*, 111–144.

Young, J.E., Boulanger-Weill, J., Williams, D.A., Woodruff, G., Buen, F., Revilla, A.C., Herrera, C., Israel, M.A., Yuan, S.H., Edland, S.D., and Goldstein, L.S. (2015). Elucidating molecular phenotypes caused by the SORL1 Alzheimer's disease genetic risk factor using human induced pluripotent stem cells. Cell Stem Cell *16*, 373–385.

Yuan, A., Veeranna, Sershen, H., Basavarajappa, B.S., Smiley, J.F., Hashim, A., Bleiwas, C., Berg, M., Guifoyle, D.N., Subbanna, S., et al. (2018). Neurofilament light interaction with GluN1 modulates neurotransmission and schizophrenia-associated behaviors. Transl. Psychiatry *8*, 167.

Zhang, B., Koh, Y.H., Beckstead, R.B., Budnik, V., Ganetzky, B., and Bellen, H.J. (1998). Synaptic vesicle size and number are regulated by a clathrin adaptor protein required for endocytosis. Neuron *21*, 1465–1475.

Zhang, K., Fishel Ben Kenan, R., Osakada, Y., Xu, W., Sinit, R.S., Chen, L., Zhao, X., Chen, J.Y., Cui, B., and Wu, C. (2013). Defective axonal transport of Rab7 GTPase results in dysregulated trophic signaling. J. Neurosci. *33*, 7451–7462.

Zhang, Z., Zhang, T., Wang, S., Gong, Z., Tang, C., Chen, J., and Ding, J. (2014). Molecular mechanism for Rabex-5 GEF activation by Rabaptin-5. eLife *3*, e02687.

Zhu, H., Zhu, G., Liu, J., Liang, Z., Zhang, X.C., and Li, G. (2007). Rabaptin-5-independent membrane targeting and Rab5 activation by Rabex-5 in the cell. Mol. Biol. Cell *18*, 4119–4128.

Zott, B., Simon, M.M., Hong, W., Unger, F., Chen-Engerer, H.J., Frosch, M.P., Sakmann, B., Walsh, D.M., and Konnerth, A. (2019). A vicious cycle of β amyloid-dependent neuronal hyperactivation. Science *365*, 559–565.

STAR★METHODS

KEY RESOURCES TABLE

REAGENT or RESOURCE	SOURCE	IDENTIFIER
Antibodies		
Mouse monoclonal anti-β-actin	Santa Cruz Biotechnology	Cat. n. sc-47778; RRID:AB_2714189
Rabbit monoclonal anti-AKT	Cell Signaling Technology	Cat. n. 4685; RRID:AB_2225340
Rabbit monoclonal anti-p-AKT^{S473}	Cell Signaling Technology	Cat. n. 4060; RRID:AB_2315049
Rabbit monoclonal anti-p-AKT^{T308}	Cell Signaling Technology	Cat. n. 2965; RRID:AB_2255933
Rabbit polyclonal anti-APPL1	Proteintech	Cat. n. 12639-1-AP, RRID:AB_2289669
Mouse monoclonal anti-APP-CTF C1/6.1	Mathews et al., 2002	N/A
Goat polyclonal anti-choline acetyltransferase	Millipore Sigma	Cat. n. AB144; RRID:AB_90650
Mouse monoclonal anti EEA1	Santa Cruz Biotechnology	Cat. n. sc-0848, RRID:AB N/A
Rabbit monoclonal anti-GluA1	Cell Signaling Technology	Cat. n. 13185; RRID:AB_2732897
Rabbit polyclonal anti-p-GluA1^{S831}	R&D Systems	Cat. n. PPS007; RRID:AB_2113595
Rabbit monoclonal anti-p-GluA1^{S845}	Cell Signaling Technology	Cat. n. 8084; RRID:AB_10860773
Mouse monoclonal anti-GluA2	ThermoFisher Scientific	Cat. n. 32-0300; RRID:AB_86910
Rabbit polyclonal anti-p-GluA2^{S880}	Abcam	Cat. n. ab52180; RRID:AB_880227
Mouse monoclonal anti-GSK-3β	Cell Signaling Technology	Cat. n. 9832; RRID:AB_10839406
Rabbit monoclonal anti-p-GSK-3β^{S9}	Cell Signaling Technology	Cat. n. 5558; RRID:AB_10013750
Rabbit polyclonal anti-p-GSK-3β^{Y216}	Abcam	Cat. n. ab75745; RRID:AB_1310290
Mouse monoclonal anti-Myc Tag (Clone 9E10)	Millipore Sigma	Cat. n. 05-419; RRID:AB_309725
Rabbit polyclonal anti Na^+/K^+ ATPase	Cell Signaling Technology	Cat. n. 3010, RRID:AB_2060983
Rabbit polyclonal anti-NHE6/SLC9A6	Bethyl Laboratories	Cat. n. A304-448A; RRID:AB_2620642
Rabbit monoclonal anti-Rab5	Abcam	Cat. n. ab109534; RRID:AB_10865740
Rabbit polyclonal anti-Rab5	Abcam	Cat. n. ab18211, RRID:AB_470264
Rabbit polyclonal anti-Rab5a	Santa Cruz Biotechnology	Cat. n. sc-309; RRID:AB_632295
Mouse monoclonal anti-Rab5-GTP	NewEast Biosciences	Cat. n. 26911; RRID:AB_2617182
Mouse monoclonal anti-Rabaptin-5	BD Biosciences	Cat. n. 610676, RRID:AB 398003
Rabbit polyclonal anti-RabGEF-1	Proteintech	Cat. n. 12735-1-AP, RRID:AB_2175788
Mouse monoclonal anti-RhoB	Santa Cruz Biotechnology	Cat. n. sc-8048, RRID:AB_628219
Rabbit polyclonal anti-Sec61B	Proteintech	Cat. n. 15087-1-AP RRID:AB_2186411
Rabbit polyclonal anti-SGSM3 (RabGAP5)	Proteintech	Cat. n. 20825-1-AP, RRID:AB_10693680
Mouse monoclonal anti-phosphorylated Tau, CP13	Kind gift of P. Davies	N/A
Mouse monoclonal anti-phosphorylated Tau, PHF-1	Kind gift of P. Davies	N/A
Rabbit polyclonal anti-total Tau	Dako Agilent	Cat. n. Cat# A0024, RRID:AB_10013724
Mouse monoclonal anti-TfR	ThermoFisher Scientific	Cat. n. 13-6800; RRID:AB_2533029
Chemicals, Peptides, and Recombinant Proteins		
Bradford	Bio-rad	Cat. n. 500-0006
GTP-agarose beads	Sigma	Cat. n. G9768
Sulfo-NHS-SS-Biotin	Pierce	Cat. n. 89881
Bis (sulfosuccinimidyl) suberate (BS3)	ThermoFisher Scientific	Cat. n. 21580
Optiprep™ Density gradient medium	Sigma-Aldrich	Cat. n. D1556

(*Continued on next page*)

Continued

REAGENT or RESOURCE	SOURCE	IDENTIFIER
Critical Commercial Assays		
DAB Peroxidase Substrate Kit	Vector Laboratories	Cat. n. SK-4100
Vectastain ABC kit	Vector Laboratories	Cat. n. PK6105
FD Rapid Golgi Stain kit	FD NeuroTechnologies	Cat. n. PK401A
Experimental Models: Organisms/Strains		
Mouse: Myc-Rab5a/ C57BL/6J	This paper	N/A
Mouse: 5XFAD	Oakley et al., 2006; M. Ohno	N/A
Oligonucleotides		
Primer Myc-Rab5-forward: 5′-GAG CAG AAG CTC ATC TCA GAA GAA GAC CTC-3′;	This paper	N/A
Primer Myc-Rab5-reverse: 5′-GTT ACT ACA ACA CTG ATT CCT GGT TGG TTG-3′	This paper	N/A
Recombinant DNA		
Plasmid: Myc-Rab5a	Kind gift of A. Cataldo	N/A
Software and Algorithms		
pClamp 10.3	Molecular Devices	https://www.moleculardevices.com
Zeiss AxioVision 4.5	Zeiss	https://www.zeiss.com/corporate/int/home.html
Fiji/ImageJ	Schindelin et al., 2012	https://imagej.nih.gov/ij/
GraphPad Prism 7	GraphPad	https://www.graphpad.com

RESOURCE AVAILABILITY

Lead Contact

Further information and requests for resources and reagents should be directed to and will be fulfilled by the Lead Contact, Dr. Ralph A. Nixon (Ralph.Nixon@NKI.RFMH.ORG).

Materials Availability

All unique reagents generated in this study are available from the Lead Contact and may require completion of a Materials Transfer Agreement.

Data and Code Availability

No custom code was used in this study.

EXPERIMENTAL MODEL AND SUBJECT DETAILS

Mouse experimentation and animal care were approved by the Nathan S. Kline Institute's Institutional Animal Care and Use Committee. Transgenic mice expressing the human Rab5a isoform selectively in neurons (PA-Rab5) were generated using the Thy1 expression cassette (Rao et al., 2008). The pTSC21 vector containing murine Thy1 expression was digested and blunt-ended, and Myc-rab5 cDNA was obtained from a pHSV-Myc-rab5 plasmid (kind gift from Dr. Anne M. Cataldo). Myc-rab5 was inserted into the Thy1 cassette by ligation. The DNA for injection was released, purified from a 10% agarose gel, dialyzed, and injected into FVB/N zygote eggs following the protocol at the transgenic mouse facility at New York University Langone Medical Center. To identify founders, PCR with tail DNA was performed. Briefly, genomic DNA obtained from tail biopsies was prepared using the DNAeasy tissue kit (QIAGEN). The following primer pairs were used; Myc-Rab5-forward 5′-GAG CAG AAG CTC ATC TCA GAA GAA GAC CTC-3′; Myc-Rab5-reverse 5′-GTT ACT ACA ACA CTG ATT CCT GGT TGG TTG-3′. PCR program for Myc-rab5 was carried out as follows: 2 m 95°C; 30 s 94°C; 30 s 55°C; 1 m 72°C; 5 m 72°C, and steps 2 to 4 were repeated 30 times. Founder PA-Rab5 mice were backcrossed for more than 10 generations to C57BL/6J (Jackson Labs, Bar Harbor, ME) to obtain a fully congenic C57BL/6J strain. PA-Rab5 bred normally in expected Mendelian ratios and did not show evidence of poor health, such as low body weight, hypo-activity in a novel environment, low activity in the home cage or absence of nest-building, poor coat appearance (such as bald patches or sores), tremors, seizures and/or other easily observed morphological abnormalities or shorter lifespan. 5XFAD mice were obtained from M. Ohno (Nathan S. Kline Institute) and genotyped as previously described (Oakley et al., 2006). Animals were housed under controlled conditions of temperature and lighting and given free access to food and water.

The age of WT and PA-Rab5 mice for electrophysiological and behavioral studies was 6 ± 0.5 months. For morphological and biochemical studies, the ages used ranged from 3 to 15 months. For analyses of dendritic spines using the Golgi impregnation method, 8.5 month-old WT, PA-Rab5 and 5XFAD were stained in parallel. Male and female mice were used.

METHOD DETAILS

Immunofluorescence and diaminobenzidine (DAB) staining

At the appropriate ages, mice were anesthetized with a mixture of ketamine (100 mg/kg BW) and xylazine (10 mg/kg BW) and transcardially perfused with 4% paraformaldehyde (PFA) in 0.1 M sodium cacodylate buffer, pH 7.4 (Electron Microscopy Sciences (EMS), Hatfield, PA). Brains were removed, post-fixed in the same fixative overnight (O/N) at 4 °C and cut into 40-μm thick sections using a vibratome. Sections for immunofluorescence labeling, were washed 3 × 10 min in permeabilization/antibody dilution buffer containing 1% bovine serum albumin (BSA), 0.05% saponin, 1% normal horse serum (NHS) in Tris-buffered saline (TBS), and blocked with 20% NHS in phosphate-buffered saline (PBS) for 1 h at room temperature. Sections were incubated with primary antibodies in antibody dilution buffer O/N at 4°C, followed by incubation with the appropriate Donkey Alexa Fluor-conjugated secondary antisera mixtures (1:300; ThermoFisher Scientific) for 1 h at room temperature. Immunolabeling of early endosomes and of myc-tagged Rab5 transgene was performed using rabbit anti-Rab5a (1:100; Santa Cruz Biotechnology) and mouse anti-Myc Tag (Clone 9E10) (1:300; Millipore Sigma), respectively. Activated Rab5 was detected using mouse anti-Rab5-GTP (1:100; NewEast Biosciences). BFCN were labeled with goat anti-choline acetyltransferase (ChAT) (1:250; Millipore Sigma). AMPA receptor subunits were labeled with rabbit anti-GluA1 (1:200; Cell Signaling Technology) and mouse anti-GluA2 (1:200; ThermoFisher Scientific), respectively. To assess cell surface GluA1 and GluA2, sections did not receive treatment with Saponin. Inactive GSK-3β was detected with rabbit anti-p-GSK-3β^{S9} (1:100; Cell Signaling Technology). Phosphorylated tau was stained with mouse anti-PHF-1 and mouse anti-CP13 (1:250; kind gifts of P. Davies). Cell nuclei were counterstained with DRAQ5 fluorescent probe for 5 min in PBS (1:2000; Thermofisher) and visualized in blue pseudocolor. Confocal imaging was performed using a plan-Apochromat 40x/1.4 oil objective lens on a LSM880 laser scanning confocal microscope (ZEISS) at a resolution of 1024 × 1024 pixels as previously described (Lee et al., 2019). DAB tissue staining was performed as previously described (Jiang et al., 2016). Briefly, sections were incubated with 3% H2O2 and 10% methanol in TBS to quench endogenous peroxidase activity, prior to permeabilization and blocking. Goat anti-ChAT (1:250; Millipore Sigma) and rabbit-anti total Tau (1:500; DAKO Agilent) primary antibodies were visualized with DAB Peroxidase Substrate Kit after incubation with biotinylated secondary antibodies (1:500) and peroxidase using the Vectastain ABC kit (all reagents from Vector Laboratories). Immunostained sections were examined with a Zeiss AxioScope at 20x and 40x magnifications and digital images were acquired using the Zeiss AxioVision 4.5 software.

Morphometric analyses

For quantification of Rab5a and Rab5-GTP positive puncta, coronal sections containing both cortex and hippocampus were used. For the cortical region, ~30-50 neurons per animal (n = 3-6/genotype) were individually analyzed from 40x magnification images with zoom value of one (212.55 × 212.55 μm^2) or 3x-zoomed (70.85 × 70.85 μm^2). For the CA1 region, Rab5 puncta in stratum pyramydale and stratum radiatum were determined from 40x magnification images containing ~30-50 neurons/field (n = 3/genotype). Image analysis was performed using Fiji/ImageJ software (Schindelin et al., 2012). Following background subtraction using a rolling ball radius of 50 and Yen's method image thresholding, Rab5 puncta intensity, size and area fraction/cell (cortex) or area fraction/field (CA1) were determined. Data are expressed as mean ± Standard Error of the Mean (SEM) relative to WT and represented as bar graphs showing individual data points for each mouse.

Rab5-GTP antibody specificity *ex vivo* was determined by colocalization analysis of Rab5a and Rab5-GTP in cortical neurons using the ImageJ software JACoP Plug-In (Jiang et al., 2019a). Rab5-GTP antibody validation for use in IF *in vitro* in non-neuronal cells has been previously shown (Mani et al., 2016) and confirmed by us in murine neuroblastoma cells based on our previous work (not shown) (Kim et al., 2016).

To measure surface and total GluA1 and GluA2 puncta, Z stacks of three 70.85 × 70.85 μm^2 1 μm-spaced optical sections of stratum pyramidale and stratum radiatum were collected and projected into a single image. For puncta quantification, all images were thresholded based on the intensity of the WT permeabilized condition to exclude background signals and to determine the relative proportions of surface to total receptors in each region. Puncta whose areas ranged from 0.005-2 μm^2 were counted and ratios of surface/total receptor were calculated. Data are expressed as mean ratios ± Standard Error of the Mean (SEM) relative to WT, or relative to the respective total counts (%), from 3 mice/genotype and represented as bar graphs showing individual data points for each mouse. Representative fields, 20.52 × 20.52 μm^2 for GluA2 and 30.10 × 30.10 μm^2 for GluA1, from the 70.85 × 70.85 μm^2 Z stack are shown in respective figures to visualize clearer puncta and total GluA immunoreactivity.

p-GSK-3β^{S9} antibody specificity for use in IF was validated *in vitro* in N2a cells untreated or treated with the archetypal GSK-3β inhibitor LiCl (Martin et al., 2018) or the selective GSK-3β inhibitor IM-12 (Ishikawa et al., 2019; Schmöle et al., 2010) (not shown). The same antibody has also been validated by others for IF of mouse tissue sections (Chow et al., 2014; Sathiya Priya et al., 2019).

Analysis of phospho-tau was carried out by cell-based measurements of PHF-1 and CP13 fluorescence intensities in layer V and layer II/III cortical neurons from 12-17 confocal images at 40x from n = 3 mice/genotype (approximately n = 260-360 cells/genotype). A similar analysis was conducted for quantification of total tau from DAB-labeled tissue sections. In this case, 21 fields at 40x

from n = 3 mice/genotype were analyzed (approximately n = 500 cells/genotype). The average perikaryal intensities of PHF-1, CP13 or total tau in each field were normalized to WT and represented as box and whisker plots. Further analysis of PHF-1 and CP13 fluorescent signals was performed by setting the average intensity of WT as a threshold, which was subtracted from the intensity of each individual cell. The number of cells above threshold and their intensity were measured. Intensity distributions of PHF-1 and CP13 above the respective thresholds were normalized to WT and represented as box and whisker plots.

Electron microscopy and immunogold EM

Electron microscopy was performed as previously described (Yang et al., 2009), with minor modifications. In brief, mice were transcardially perfused with 4% PFA supplemented with 2% glutaraldehyde in 0.1 M sodium cacodylate buffer, pH 7.4. Brains were cut into 80 μm-thick sagittal vibratome sections and post-fixed in 1% osmium tetroxide. Following alcohol dehydration, sections were infiltrated with increasing concentrations of Spurr resin and flat embedded in Aclar sheets. Regions of interest for ultrastructural analyses, including pre-frontal cortex and hippocampal CA1 and Dentate Gyrus areas, were cut out and 50 nm ultrathin sections were prepared and stained with uranyl acetate and lead citrate. The material was viewed with a Thermo Fisher Talos L120C transmission electron microscope operating at 120kV. For endosome quantification, approximately n = 60 EM images (17,500X) per mouse per genotype (WT n = 5; PA-Rab5 n = 4), containing dendritic and synaptic profiles in the proximity (within 5-10 μm) of the neuronal soma were acquired from the pyramidal cell layer V of the pre-frontal cortex. Endosomes were counted and the average diameter distributions within the indicated bins and the endosome area fraction relative to the total image area were determined for each mouse/genotype using Fiji/ImageJ (Schindelin et al., 2012). For ultrastructural analysis of hippocampal dendritic spine morphologies (non-stubby and stubby) in the CA1 stratum radiatum, only profiles with spine heads and necks entirely on the plane of the section were counted from random fields acquired at 5,300X (WT n images, spines = 22, 127; PA-Rab5 n images, spines = 23, 149). Results are expressed as mean ± SEM (% of non-stubby and stubby profiles relative to the total counts per image/genotype) and represented as bar graphs showing individual data points of the. Post-embedding immunogold EM was performed using a previously described protocol (Yang et al., 2009). Briefly, ultrathin sections were mounted on nickel grids, air-dried, and etched 5 min with 1% sodium metaperiodate in PBS followed by washing in filtered double-distilled water and incubated with 1% BSA in PBS for 2 h. Sections then were incubated O/N with mouse monoclonal anti-Rab5-GTP (1:30, NewEast Biosciences), rabbit monoclonal anti-Rab5 (1:30; Abcam) and rabbit polyclonal anti-NHE6/SLC9A6 (1:30; Bethyl Laboratories) in a humidified chamber O/N at 4 °C, washed in PBS, and incubated with 6- and 10-nm gold-conjugated anti-mouse and anti-rabbit secondary antibodies, respectively, for 2 h at room temperature. Mouse or rabbit IgG isotype control sections were prepared in parallel by omitting the primary antibody. Grids were washed and briefly stained with uranyl acetate and lead citrate before imaging, which included examination of other organelles as well (e. g. mitochondria and multivesicular bodies), besides endosomes, to ensure labeling specificity.

Electrophysiology

6-month-old male and female mice (n = 8 mice/genotype) were sacrificed by cervical dislocation followed by decapitation. Hippocampi were quickly removed. Transverse hippocampal slices (400 μm) were cut and recorded according to standard procedures (Joshi et al., 2019; Subbanna et al., 2013). Briefly, hippocampal slices maintained at 29°C were perfused with artificial cerebrospinal fluid (ACSF, composition in mM: 124.0 NaCl, 4.4 KCl, 1.0 Na_2HPO_4, 25.0 $NaHCO_3$, 2.0 $CaCl_2$, 2.0 $MgSO_4$, 10.0 glucose, osmolarity 290–300) continuously bubbled with 95% O_2 and 5% CO_2. CA1 field excitatory postsynaptic potentials (fEPSPs) were recorded by placing both the stimulating and the recording electrodes in CA1 stratum radiatum. Basal synaptic transmission was assessed by plotting the stimulus voltages against slopes of field-excitatory-post-synaptic potential (fEPSP). For LTP and LTD experiments, a 10 min baseline was recorded at 1 min intervals at an intensity that evokes a response ~35% of the maximum evoked response. LTP was induced by using theta-burst stimulation (4 pulses at 100 Hz, with the bursts repeated at 5 Hz, and each tetanus including three 10 burst trains separated by 15 s) and LTD was induced using 1Hz for 900 s. Responses were recorded for 2 hours (LTP) or 80 min (LTD) after and measured as fEPSP slope expressed as a percentage of baseline. The results are expressed as mean ± SEM and represented as bar graphs showing individual data point.

Novel Object recognition

Novel object recognition memory was evaluated as described before (Subbanna et al., 2013). The test was carried out in a 40 × 40 cm open field surrounded by 20 cm high walls made of Plexiglass (Stoelting, Wood Dale, IL USA). 6 month-old male and female WT (n = 12) and PA-Rab5 (n = 9) mice were submitted to a habituation session where they were allowed to freely explore the open field for 5 min × 2 for two days. No objects were placed in the box during the habituation trial. Twenty-four hours after habituation, training (T1) was conducted by placing individual mice for 3 min in the open field, in which two identical objects (A) were positioned in two adjacent corners at 10 cm from the walls. A long-term recognition memory test was given at 24h (retention) after training (T2) during which the mice explored the open field for 3 min in the presence of one familiar (A) and one novel (B) object. All combinations and locations (left and right) of the objects were used in a balanced manner in order to reduce potential biases due to particular location or objects preferences. All objects had similar textures and sizes but had distinctive shapes and colors (Stoelting, Wood Dale, IL USA). Between trials, the objects were washed with 10% ethanol solution. Exploration was defined as directing the nose to the object at a distance of no more than 2 cm and/or touching the object with the nose. Sitting on the object was not considered as exploratory behavior. e1 and e2 are measures of the total exploration time of both objects during T1 and T2, respectively. The Recognition index (RI), or

preference score, is calculated as RI = [time exploring the novel object)/(time exploring novel + familiar)]. RI appears to be independent of the total exploration times. The times spent exploring each object during T1 and T2 were recorded manually with a personal computer.

Golgi staining for spine density and morphology

Golgi staining was performed using the FD Rapid Golgi Stain kit (FD NeuroTechnologies) as previously described (Yuan et al., 2018). Spines were sampled on 3-4 dendrites on each of 3 cells per area, per animal, in the dorsal hippocampus. CA1 and CA3 pyramidal cells were sampled in the stratum radiatum at terminal ends of dendrites that branched off the apical dendrites. Dentate granule cells were sampled near the surface of the stratum moleculare at terminal ends of dendrites. Spine density was measured on 50-80 μm dendritic lengths, in 3-dimensional image stacks that were 20 μm deep with 0.66 μm slice spacing, acquired with a Foculus F0442 digital camera (Net GMBH, Germany) with a 100x, 1.3 numerical aperature oil objective and a motorized Nikon E600 microscope. Every 5th spine counted was measured for length (distance from dendrite center to spine tip) using ImageJ software (https://imagej.nih.gov/ij). Cumulative distribution curves of spine lengths were generated using GraphPad Prism 7.

Stereological counting of MSN-ChAT cells

The number of ChAT-immunoreactive BFCNs in the MSN was stereologically determined using the optical fractionator method and analyzed using ImageJ software (https://imagej.nih.gov/ij), as previously described (Jiang et al., 2016). The MSN was sampled dorsal to the ventral edge of the anterior commissure, in every third consecutive section rostral to the commissure. Sections were sampled with a grid of optical dissector counting sites. At each site, a 40x oil immersion objective was used to collect a z stack of seven 2-μm-spaced images. A 160 × 116 μm counting box was drawn onto each z stack, with an upper guard zone of 2 μm (1 slice), counting box of 4 μm, and lower guard zone made of the remaining z-slices. Cell counts were corrected for z axis shrinkage in each brain. Section thickness was 9.35 ± 0.25 μm (mean ± standard deviation [SD]) and did not differ between genotype (two-tailed Student's t test; $t_{(10)}$ = 1.049, p = 0.319). On average, 337 ± 33 cells were counted per MSN, and the coefficient of error was 0.059 ± 0.005 (mean ± SD).

Surface biotinylation of acute hippocampal slices and sample homogenization for biochemical analysis

Surface biotinylation of acute hippocampal slices was performed as described in Thomas-Crusells et al. (2003), with minor modifications. Briefly, using two 60 mm x 15 mm Petri dishes containing tissue culture filters, eight to ten x 400 μm hippocampal slices (obtained as described above) per filter per mouse (n = 4 independent labeling reactions/genotype) were maintained in ACSF for 1h at room temperature, followed by 2 washes of iced-cold ACSF to chill the slices prior to surface biotinylation. Slices were then incubated with 0.5 mg/ml Sulfo-NHS-SS-Biotin (Pierce) for 45 min in ice. Excess biotin was removed by 2 washes with ice-cold 50 mM NH_4Cl in ACSF (quenching buffer) prior to slice homogenization and biochemical analysis. To control for receptor internalization (not shown), in a separate set of experiments we performed chemical stimulation with Glutamate (Sigma) using a two-chamber perfusion, as method validation (Thomas-Crusells et al., 2003). In this case, slices were equilibrated at room temperature for 1h before perfusion with ACSF (maintained at 28-29°C). After ACSF perfusion for 40 min, one chamber was perfused with 500 μM Glutamate for 60 min and the other was perfused with ACSF alone. The following washes and surface labeling steps were performed as described above. Slices were immediately homogenized in 0.5 mL of lysis buffer (150 mM NaCl, 20 mM HEPES, 1% Triton X-100, 0.1% SDS, 2 mM EDTA pH 7.4, and protease/phosphatase inhibitors) and centrifuged at 15,000 x g for 5 min to remove debris. An aliquot of the supernatant (~40 μl) was saved as total input. 1 mg of lysed biotinylated samples in 400 μL of lysis buffer was incubated with washed Streptavidin Magnetic Beads (Pure Proteome Streptavidin Magnetic Beads, Millipore) under rotation O/N at 4°C. After magnet application, the supernatant was removed, and the beads washed three times with lysis buffer. After removal of residual lysis buffer, beads were eluted with 45 μL of 1 × Laemmli sample buffer and heated at 90°C for 5 min. The eluted fraction, representing the biotinylated surface proteins, was collected after magnet application and processed along with ~2% of the total initial proteins for Western Blot analysis. Total proteins were normalized against actin and biotinylated surface proteins against Transferrin receptor (TfR). Relative surface/total receptor ratios were calculated for each genotype and results normalized to WT samples.

Synaptosome isolation

Synaptosomes (SS) were isolated from WT and PA-Rab5 mouse hippocampi (n = 8 hippocampi per mouse/ genotype) by homogenization in 250 μL of a sucrose solution (0.32 mol/L sucrose, 0.1 mmol/L $CaCl_2$, 1 mmol/L $MgCl_2$) with protease and phosphatase inhibitors (5 μg/ml Pepstatin A, 5 μM Leupeptin, 1mM AEBSF, 1 ng/ml Microcystin as previously described (Louneva et al., 2008). Briefly, after homogenization, samples were adjusted to 1.25 M and sequentially overlaid with 1.0 M Sucrose in 0.1 mM $CaCl_2$ and homogenization buffer. Following sample centrifugation at 100,000 x g (32,500 RPM) for 3 h at 4°C using a SW55Ti rotor (Beckman Coulter), the interface at 1.25-1.0 M sucrose, enriched in SS, was diluted in ice-cold 0.1 mM $CaCl_2$, centrifuged at 75,000 x g (28,000 RPM) for 30 min at 4°C in a SW55Ti rotor and the pellets washed in 0.1 mM $CaCl_2$ and centrifuged again. The washed SS pellets were either processed for Rab5-GTP pull down assays (see below) or further extracted to separate SS soluble/cytosolic (SScyt), pre- and postsynaptic fractions using the method of Phillips (Phillips et al., 2001). Briefly, SS were extracted in 20 mM Tris-HCl, pH 6.0 containing 0.1 mM $CaCl_2$, 1% Triton X-100, protease and phosphatase inhibitors for 30 min on ice and centrifuged at 34,000 x g (19,000 RPM) for 30 min at 4°C. The resultant supernatant represented the SScyt fraction. The respective pellet was resuspended in 20 mM Tris-HCl, pH 8.0 containing 0.1 mM CaCl2, 1% Triton X-100, and protease and phosphatase inhibitors for

30 min on ice and centrifuged at 34,000 x g (19,000 RPM) for 30 min at 4°C. The resultant supernatant represented the pre-synaptic membrane (PRSM) and the pellet the post-synaptic density (PSD) membrane. SScyt and PRSM fractions were precipitated with acetone. All fractions were dissolved in 8M Urea, boiled for 5 min in 5x Laemmli sample buffer and ran on 12% polyacrylamide SDS-PAGE gels. Specific protein bands were normalized against Ponceau.

Rab5-GTP pull-down assays from hippocampal homogenates and synaptosomes

The amount of Rab5-GTP was assayed in total hippocampal homogenates and SS preparations by two methods: 1) by GTP-Agarose pull-down (Fang et al., 2017; Xu et al., 2016; Zhang et al., 2013); 2) by immunoprecipitation (IP) with the Rab5-GTP antibody (modified protocol from NewEast Biosciences Rab5 activation assay kit cat. N. 8370). The GTP-agarose pull down assay measures the levels of GTP-bound Rab5, by reflecting the guanine nucleotide exchange activity of a GEF protein (e.g., RabGEF-1) toward Rab5 (Shi et al., 2018). For this assay, mouse hippocampi were lysed in GTP-Agarose lysis/wash buffer (50 mM Tris-HCl pH 7.5, 250 mM NaCl, 5 mM Mg acetate, 0.5% Triton X-100, and protease inhibitors), followed by centrifugation at 13,000 x g for 10 min at 4°C. An aliquot of supernatants (30 μl) was saved as the loading control and ~0.5-1 mg were incubated with 300 μL of GTP-agarose beads (Sigma Cat# G9768) for 4h at 4°C with rotation. Alternatively, SS pellets, isolated as described above, were resuspended in GTP-Agarose lysis buffer, incubated on ice for 30 min and sonicated. After saving an aliquot as loading control, ~0.2 mg of SS proteins were incubated with 300 μL GTP-agarose beads O/N at 4°C with rotation. For IP, isolated SS were homogenized in IP/wash buffer (50 mM Tris, pH 7.4, 150 mM NaCl, 1mM $MgCl_2$, 1 mM EDTA, 1% Triton), incubated on ice for 30 min and sonicated. After saving an aliquot, ~0.2 mg of SS proteins in 300 μL of IP/wash buffer were incubated with anti-Rab5-GTP-, or Normal Mouse IgG (negative control)- crosslinked PureProteome™ Protein A/G Magnetic beads (Millipore Sigma) O/N at 4°C with rotation. The cross-linking reaction was carried out to minimize co-IP of non-specific IgG in amine-free buffer using bis (sulfosuccinimidyl) suberate (BS3), following the manufacturer's instructions (ThermoFisher Scientific). A separate reaction was carried out in the presence of 10 μM GTPγS, a non-hydrolyzable G-protein-activating analog of GTP, at 30°C for 30 min, prior to IP to stabilize active Rab5 (positive control). The same reaction in the GTP-Agarose pull-down assay served to control for specific binding. The beads were then washed with respective wash buffer, resuspended in Laemmli sample buffer and boiled. The amount of Rab5-GTP was measured following SDS-PAGE and blotting with an anti-Rab5 antibody and the results expressed as Rab5-GTP/total rab5.

Hippocampal endosome-enriched cytosol (EEcyt) preparation for Rab5-GTP and RabGEF-1 IP

Mice were anesthetized as described above and transcardially perfused with phosphate-buffered saline solution. Hippocampi were homogenized in 1:10 w/v homogenization buffer (HB, 0.25 M Sucrose, 10 mM Tris-HCl pH 7.4, 1 mM EDTA, protease and phosphatase inhibitors) by 10 strokes of a Teflon-coated pestle. Nuclei and unbroken material were pelleted by centrifugation at 800 g for 20 min at 4°C to obtain a post-nuclear supernatant (PNS). The PNS was then centrifuged at 16,000 x g for 20 min at 4°C to pellet heavy membranes and the resultant endosome-enriched cytosol (EEcyt) was diluted in 3X detergent-free IP buffer (150 mM Tris-HCl, pH 7.4, 450 mM NaCl, 3 mM MgCl2, 3mM EDTA with protease and phosphatase inhibitors). Approximately 3-5 μg of Rab5-GTP and RabGEF-1 antibodies were used for 200 μg of EEcyt in IP buffer: 1) For Rab5-GTP IP, the antibody/EEcyt mixture was incubated with PureProteomeTM Protein A/G Magnetic beads (Millipore Sigma) O/N at 4°C with rotation; 2) For RabGEF-1 (Proteintech, cat. n.12735-1-AP) IP, the antibody was first immobilized onto the magnetic beads by 30 min incubation at 4°C, followed by the addition of the EEcyt and 1h incubation at 4°C with rotation to minimize GTP hydrolysis for RabGEF-1/Rab5 complex detection. Each IP experiment included positive (10 μM GTPγS) and negative (normal mouse or rabbit IgG) control reactions, as described above. Following the antibody-sample/bead incubation, a magnet was applied, the supernatant removed, and the beads were washed three times with 1X IP buffer containing 0.1% Triton X-100. Samples were eluted with 2X Laemmli sample buffer, heated for 5 min at 95°C, followed by western blot analysis and detection with Rab5 and RabGEF-1 antibodies.

Endosome isolation

Endosomes were isolated from mouse cortical PNS obtained as described above. 4 mg of PNS proteins were adjusted to 25% OptiPrep with a 50% OptiPrep stock in HB to a final volume of 2 ml. The resulting mixture was placed at the bottom of an open-top thin-wall ultracentrifuge tube (14 × 89mm, Beckman Coulter) and sequentially layered with 1.5 mL of 20%, 15%, 14%, 12.5%, 10% and 5% OptiPrep in cold HB. The gradients were centrifuged for 16 h at 27,000 rpm at 4°C in a rotor (SW 41 Ti; Beckman Coulter) and 20 × 0.55 mL fractions were collected from the bottom using a peristaltic pump for initial western blot profiling (equal fraction volumes were analyzed). Fractions #1-4 and #13-17, enriched in cytosol (Cyt) and endosomes (EE), respectively, were subsequently pooled, precipitated overnight in 7% (v/v) trichloroacetic acid (TCA) at -20°C and resuspended in a 1:1 mixture of 8M Urea and 10 mM Tris-HCl, pH 7.4, 1% NP-40, 1% Na-deoxycholate, 2% SDS. Equal amounts of PNS, Cyt and EE proteins were separated by western blot as described below.

Tissue preparation for Western Blot and ELISA and primary antibodies

Mice were anesthetized and perfused as described above. Brains were removed and cortical and hippocampal regions dissected out and homogenized in 1:10 (brain weight: buffer volume) tissue homogenization buffer (250 mM sucrose, 20 mM Tris-HCl, pH 7.4, 1 mM EDTA, 1 mM EGTA, and protease/phosphatase inhibitors) as previously described (Schmidt et al., 2005). Proteins were determined with the method of Bradford (Bio-rad), and equal amounts were separated on 20- or 26-well Novex™ 4%–20% Tris-Glycine SDS-

PAGE gels or 15-well 16% Tricine protein gels (both from ThermoFisher Scientific) for separation of APP metabolites. Gels were transferred onto nitrocellulose membranes and blots were probed with primary antibodies O/N at 4°C, followed by HRP-conjugated secondary antibodies for 1 h at room temperature. The following primary antibodies were used: rabbit anti-Rab5a (1:1000, Santa Cruz Biotechnology); rabbit polyclonal anti-Rab5 (1:1000; Abcam); mouse anti-Myc-Tag, clone 9E10 (1:1000, Millipore Sigma). The majority of this study was performed using anti-Rab5a (cat n. sc-309) rabbit mapping within the C terminus of Rab5a, that is no longer commercially available. We have evaluated Abcam (cat n. ab18211/Rab5 pan-specific) as a viable substitute and will continue to investigate suitable alternatives in future studies. Additional antibodies included: mouse monoclonal anti-Rabaptin-5 (1:1000; BD Biosciences); rabbit polyclonal anti-RabGEF-1 (1:1000; Proteintech); mouse monoclonal anti-RhoB (1:1000; Santa Cruz); rabbit anti-GluA1 (1:1000; Cell Signaling Technology); rabbit anti-p-GluA1^{S831} (1:300; R&D Systems); rabbit anti-p-GluA1^{S845} (1:1000; Cell Signaling Technology); mouse anti-GluA2 (1:1000; ThermoFisher Scientific); rabbit anti-p-GluA2^{S880} (1:500; Abcam); mouse anti-TfR (1:1000; ThermoFisher Scientific); rabbit anti-AKT (1:1000; Cell Signaling Technology); rabbit anti-p-AKT^{S473} (1:1000; Cell Signaling Technology); p-AKT^{T308} (1:1000; Cell Signaling Technology); mouse anti-GSK-3β (1:1000; Cell Signaling Technology); rabbit anti-p-GSK-3β^{S9} (1:1000; Cell Signaling Technology); rabbit anti-p-GSK-3β^{Y216} (1:1000; Abcam); rabbit anti-total Tau (1:500; DAKO Agilent); mouse anti APP-CTF C1/6.1 (1:500) (Mathews et al., 2002); mouse anti-β-actin (1:1000; Santa Cruz Biotechnology). Immunoreactive bands in the bulk of the results were visualized by enhanced chemiluminescence (ECL, ThermoFisher Scientific) and film detection. Analyses of Rab5 and total tau expression were carried out by both ECL/film and digital gel imager (Syngene G:Box XX9) systems. All images were captured within the linear range of the signal and produced similar results between the two methods. Band intensities were quantified using Fiji/ImageJ or Multigauge ver. 5.2 software (Fujifilm).

Sandwich ELISA

Following diethylamine-extraction of cortical tissue, murine Aβ quantification was performed by ELISA as previously described (Jiang et al., 2016). Briefly, mAb JRF/cAβ40/10 or JRF/cAβ42/26 were used to capture Aβ ending at residue 40 or 42, respectively, followed by detection with horseradish peroxidase (HRP)-conjugated mAb JRF/rAβ1–15/2 for murine Aβ. The dilution JRF/rAβ1–15/2 and samples was optimized to detect Aβ in the range of 6.25 to 100 fmol ml^{-1}. ELISA signals were reported in fmol Aβ per g of brain tissue, based on standard curves using synthetic Aβ1–40 and Aβ1–42 peptide standards (American Peptide Co. Sunnyvale, CA).

QUANTIFICATION AND STATISTICAL ANALYSIS

Significance was determined using unpaired two-tailed Student's t test for single comparisons, one-way ANOVA with Sidak's or Tukey's post hoc tests for multiple comparisons, or one-way ANOVA with Dunnett's post hoc test to compare every mean with a control mean, when appropriate, using GraphPad Prism 7. Data distribution was assumed to be normal, but this was not formally tested. Most data are expressed as mean ± SEM and represented as bar graphs showing individual data points. Alternatively, data were represented as box and whisker plots, with the box extending from the 25th to the 75th percentiles and the median shown as a line, group means shown as crosses and whiskers indicating the smallest and largest values. The variance was similar between groups being statistically compared. A $p < 0.05$ was considered significant (*$p < 0.05$, **$p < 0.01$, ***$p < 0.001$, ****$p < 0.0001$). No statistical methods were used to predetermine sample sizes, but our sample sizes are similar to those reported in previous publications (Cataldo et al., 2000, 2008; Jiang et al., 2016; Subbanna et al., 2013; Yang et al., 2009). No data were excluded and all the reported data were reliably reproduced. For each figure, samples sizes, *P value*s and statistical methods are defined in the respective figure legends.